Computers and Geotechnics 170 (2024) 106294

Contents lists available at ScienceDirect

Computers and Geotechnics

journal homepage: www.elsevier.com/locate/compgeo

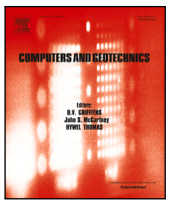

Research paper

Estimation of macroscopic failure strength of heterogeneous geomaterials containing inclusion and pore with artificial neural network approach

Jing Xue [a,b], Yajun Cao [a], Zhenyu Yin [d], Jianfu Shao [a,b,c,*], Nicolas Burlion [b]

[a] Key Laboratory of Ministry of Education for Geomechanics and Embankment Engineering, Hohai University, Nanjing, 210098, China
[b] University of Lille, CNRS, Centrale Lille, LaMcube, UMR9013, 59000 Lille, France
[c] Institut Universitaire de France, France
[d] Department of Civil and Environmental Engineering, The Hong Kong Polytechnic University, Hung Hom, Kowloon, Hong Kong, China

ARTICLE INFO

Keywords:
Failure strength
Direct numerical simulation
Artificial neural network
Heterogeneous materials
Concrete
Rocks

ABSTRACT

This work is devoted to estimation of macroscopic failure strength of heterogeneous rock-like and cement-based materials. Three representative microstructures are considered, respectively with a random distribution of pores, stiff inclusions, and both pores and inclusions in a pressure-sensitive plastic solid matrix. In the first part, a series of direct numerical simulations are performed by using a nonlinear fast Fourier transform (FFT) method. Different values of porosity and inclusion volume fraction are considered. The respective influences of pores, inclusions and their interactions on the macroscopic failure stresses are investigated for a large range of mean stress. The obtained results provides a new insight on the effect of interaction between pores and inclusion at the same scale. For this case, it is very difficult to obtain analytical solutions. In the second part, a specific model based on artificial neural network (ANN) is constructed for the prediction of macroscopic failure strength by using porosity and inclusion volume fraction as input parameters. This model is trained by using a dataset based on the results obtained from the numerical simulations. The accuracy of the ANN-based model is verified through different statistic indicators. The good performance of this model is finally shown through the comparisons between its predictions and the references solutions from the direct numerical simulations for three groups of heterogeneous materials.

1. Introduction

Cement-based and rock-like materials are widely encountered in many engineering fields. These materials contain different kinds of heterogeneity such as pores and inclusions (aggregates) at different scales (Robinet et al., 2012; Ma et al., 2021). Their macroscopic mechanical and physical properties are inherently affected by the micro-structural heterogeneity and evolution due to aging and chemical degradation. The estimation of macroscopic elastic properties, failure strength, permeability and other parameters with the micro-structural evolution is a fundamental issue for the safety and durability analysis of engineering structures. On the other hand, in the case of cement-based materials, the microstructure is directly related to mineral composition (cement, water, sand, aggregate, additive) and fabrication process. For green construction, geopolymer-based concrete is more and more used (Zailan et al., 2022; Li et al., 2022). For an optimal design of those new materials, it is needed to establish the relationships between macroscopic properties and microstructures which are related to compositions and fabrication technology. In this context, the present work focuses on the estimation of macroscopic failure strength as functions of porosity and inclusion volume fraction.

In the last decades, by using limit analysis technique and variational approach, a high number of analytical macroscopic strength criteria have been developed for different types of porous materials. We can mention the pioneer work by Gurson (1977) for porous materials with Mises type solid matrix and spherical pores. Many extensions have been proposed so far. For example, some authors have considered non-spherical voids (Gologanu et al., 1993; Monchiet et al., 2014), nonoporous materials (Brach et al., 2017) and combined effect of pore size and shape (Monchiet and Kondo, 2013), anisotropy in tension and compression (Cazacu et al., 2010; N'souglo et al., 2020), plastic anisotropic materials containing spheroidal voids (Monchiet et al., 2008), etc. Some analytical strength criteria have also been developed for porous materials with two families of voids at different scales (Vincent et al., 2009; Shen et al., 2014). Macroscopic strength criteria of heterogeneous materials reinforced by stiff inclusions have also been investigated (Gărăjeu and Suquet, 1997). For rock-like and concrete

* Corresponding author at: University of Lille, CNRS, Centrale Lille, LaMcube, UMR9013, 59000 Lille, France.
E-mail address: jian-fu.shao@polytech-lille.fr (J. Shao).

https://doi.org/10.1016/j.compgeo.2024.106294
Received 23 January 2024; Received in revised form 17 March 2024; Accepted 28 March 2024
Available online 9 April 2024

materials, a two-step homogenization technique was used to take into account the effects of pores and inclusions on two different scales (Shen et al., 2013, 2012; He et al., 2013). Based on a three-step homogenization procedure, the effect of carbonation of cement past was taken into account in an analytical strength criterion (Ghorbanbeigi et al., 2016). These analytical models provide explicit strength criteria as functions of porosity and inclusion volume fraction. Their formulation is generally based on idealized representative volume element (RVE). The real spatial distribution of pores and inclusions is not directly taken into account. The case of simultaneous presence of voids and inclusion at the same scale has been investigated in few studies and different kinds of approximation were adopted (Shen, 2022). As an alternative to analytical models, various numerical homogenization techniques have also been developed, based on direct simulations of microstructures, by using different types of numerical methods such as finite element method (FEM), discrete element method (DEM), and fast Fourier transform (FFT) solution. The numerical models are able to consider realistic microstructures but requires a high computing time. Their application to engineering problems is not obvious.

During the recent years, machine-learning based approaches, particularly those centered on artificial neural networks (ANNs), have witnessed increasing adoption in materials science and engineering applications. The remarkable adaptability of ANNs has been pivotal in their widespread acceptance, allowing them to flexibly address various challenges through parameter and hyperparameter adjustments. Unlike traditional numerical simulation models, once a machine learning model is constructed, the output can be obtained quickly based on the input. With the advancement of machine learning, there is no longer a need for tedious coding and extensive background knowledge, which significantly enhances materials science research. ANNs have found application across diverse domains, encompassing solutions for forward and inverse problems governed by partial differential equations (PDEs) (Raissi et al., 2019; Han et al., 2017; Sirignano and Spiliopoulos, 2018), reduced-order modeling (Hesthaven and Ubbiali, 2018; Lee and Carlberg, 2020; Fresca et al., 2021), and data-driven discovery (Ray and Hesthaven, 2018). They have also been instrumental in estimating material mechanical properties, including the elastic modulus of concrete (Xue et al., 2023a,b) and the uniaxial compression strength (Asteris and Mokos, 2020; Armaghani and Asteris, 2021; Gül et al., 2021), among others. Hybrid models, combining ANNs with meta-heuristic algorithms, have emerged to bolster numerical efficiency in predicting material behavior (Asteris and Mokos, 2020; Armaghani and Asteris, 2021; Gül et al., 2021). Furthermore, the development of convolutional neural networks has facilitated the modeling of structure–property relationships, notably predicting yield surfaces from microstructure images (Heidenreich et al., 2023). Similarly, neural network-based material cells have been crafted to characterize elastoplastic behavior, supporting finite element analyses in boundary value problems (Shaoheng et al., 2023). Additionally, innovative approaches such as machine learning-driven stress integration methods have been proposed for anisotropic plasticity in sheet metal forming, showcasing the versatility of machine learning models in diverse scenarios (Piemaan and Whan, 2023). Recent studies have demonstrated the potential of ANNs in various applications. These works have explored computational homogenization of materials (Le et al., 2015), development of smart constitutive laws (Logarzo et al., 2021), and investigation of deep learning-based upscaling methods (Ma and Zhang, 2023), among other areas (Vasilyeva and Tyrylgin, 2021; Vasilyeva et al., 2020; Zhang et al., 2023). However, despite these advancements, a notable challenge remains in research pertaining to the estimation of failure strength in heterogeneous materials containing pores and inclusions at the same scale and under multi-axial conditions.

The paper has two main objectives. Firstly, through a series of direct numerical simulations using the nonlinear FFT method, we investigate the influence of varying porosity and inclusion volume fractions on macroscopic failure stress. We explore the effects of pores, inclusions, and their interactions under different mean stresses, providing new insights into the interactions between pores and inclusions at the same scale. Secondly, we establish a specific model based on ANN. This model utilizes porosity and inclusion volume fraction as input parameters to estimate the macroscopic failure strength of concrete-like or rock materials with random distributions of pores and inclusions at the same microscopic scale.

For this purpose, the following methodology is adopted. In Section 2, we shall perform direct numerical simulations of RVE for three representative families of materials: porous materials, inclucion-reinforced composites, and heterogeneous materials containing both pores and inclusions. The effects of pores, inclusions and their interaction will be investigated in detail. In Section 3, a specific ANNs-based model is constructed in view of estimating macroscopic failure stresses of three types of heterogeneous materials. The structure and effectiveness of the model is presented and demonstrated by a series of benchmark test cases. The application of ANNs-based model to predicting the macroscopic failures stresses of like-concrete materials is presented Section 4. Some concluding remarks are formulated in Section 5.

2. Direct numerical simulations

In order to develop an artificial neural network (ANN) model, it is primordial to construct a large and representative dataset. It is strongly desired to collect experimental data. However, in the case of heterogeneous materials, it is very difficult to obtain a comprehensive set of experimental data for various configurations of micro-structure. In this work, an alternative approach is adopted. Direct numerical simulations (DNS) are performed on the selected representative volume element (RVE) and the obtained results are used for the construction of dataset. In order to easily account for different types of microstructures inside the RVE, in particular the spatial distribution of pores and inclusions, a numerical method based on fast Fourier transform (FFT) solution is adopted. Indeed, with this method, there is no need to create complex mesh. It is then particularly suitable for three-dimensional analysis of heterogeneous materials. The theoretical background and numerical implementation algorithm have been presented in a number of previous studies, for instance for nonlinear heterogeneous materials (Moulinec and Suquet, 1994, 1998). This method has also been successfully applied to rock and concrete materials (Cao et al., 2018; Xue et al., 2023a,b). Details of the FFT-based homogenization method for nonlinear rock-like materials have been presented in Cao et al. (2018, 2020).

In this work, we consider a class of heterogeneous materials, encompassing both man-made composites, rocks and concrete. It is also useful to point out that there are some common points of microstructures for those materials, which are mainly composed of a solid matrix in which embedded pores and inclusions. In the field of civil engineering, the primary application is for rocks and concrete. For this purpose, a typical microstructure is here selected, as shown in Fig. 1. For the sake of simplicity but without loosing generality, spherical pores and inclusions are considered here. It is noticed that the modeling method presented here can also be easily applied to non-spherical inclusions and pores.

The matrix phase exhibits an elastic perfectly plastic behavior while the inclusions are characterized by a linear elastic model. We focus here on typical materials used in civil engineering applications, such as concrete and rocks. It is known that the plastic behavior of those materials is strongly dependent on mean stress. Therefore, the local plastic yield condition of the matrix phase is here described by the widely used Drucker–Prager criterion:

$$F^m = \widetilde{\sigma}_d + T(\widetilde{\sigma}_m - h) \leqslant 0 \tag{1}$$

By denoting $\widetilde{\boldsymbol{\sigma}}$ as the local stress tensor inside the matrix phase, $\widetilde{\sigma}_m = tr\widetilde{\boldsymbol{\sigma}}/3$ is the mean stress while $\widetilde{\sigma}_d$ is the deviatoric stress defined as $\widetilde{\sigma}_d = \sqrt{\frac{3}{2}\widetilde{\boldsymbol{\sigma}}' : \widetilde{\boldsymbol{\sigma}}'}$, with $\widetilde{\boldsymbol{\sigma}}'$ being the deviatoric stress tensor. The parameter T

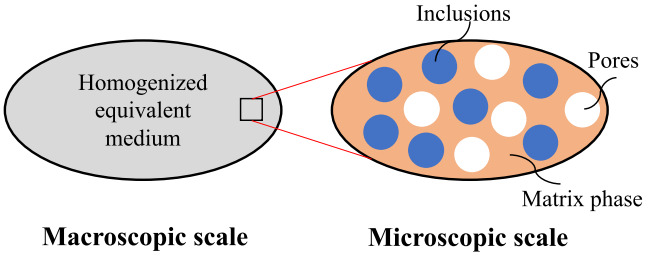

Fig. 1. Representative volume element of studied heterogeneous materials.

Table 1
Mechanical properties of constituents.

	Young's modulus	Poisson's ratio	Frictional coefficient	Hydrostatic Tensile strength
Matrix	E_m = 13.4 GPa	ν_m = 0.25	T = 0.9	h = 5 MPa
Inclusions	E_i = 74.5 GPa	ν_i = 0.15		

represents the local frictional coefficient and h the hydrostatic tensile strength of the solid matrix at the microscopic scale.

In the direct simulation with the FFT-based method, the RVE is represented by a cubic unit cell subjected to periodic conditions. A specific number of spheres of uniform size are randomly embedded within the unit cell at fixed positions. Inclusions and pores are differentiated by assigning distinct elastic parameter values to their respective spheres. Consequently, the volume occupied by the spheres (whether pores or inclusions) is calculated based on the sphere radius and quantity. Notably, for simplicity, this paper initially overlooks the size effects of pores and inclusions. The spatial resolution for all calculations presented here is fixed to 150 × 150 × 150 voxels. Additionally, the influence of the spatial location of inclusions and pores on the numerical results is well worth exploring. To this end, we randomly generated three types of microstructures, namely Microstructure-A, Microstructure-B, and Microstructure-C. Their differences lie in the distribution of pore and inclusion spatial positions. The common factors among them are a porosity of $f = 20\%$, an inclusion volume fraction of $\rho = 20\%$, and a total number of inclusions and pores $N = 300$. Fig. 2 depicts the three microstructures of the model and their corresponding stress–strain curves under a confining pressure of −10 MPa. It can be observed that the different distributions of inclusions and pores have a certain impact on the failure strength. To mitigate this uncertainty, in addition to ensuring fixed spatial positions for the spheres, it is necessary to assign a unique sequence number to each sphere. During each microstructure generation, the spheres are designated as either pores or inclusions in a rigorously sequential order based on their assigned sequence numbers, pores are prioritized over inclusions in this paper. This ensures the completion of microstructure parameterization, where the fixed volume fractions of porosity and inclusions correspond to a unique microstructure. In the subsequent research, unless otherwise specified, the spatial positions and sequence numbers of the spheres in the microstructures generated by FFT are based on Microstructure-A, as shown Fig. 2(a).

The emphasis is to put on the effect of porosity and inclusion fraction on the macroscopic failure strength. The mechanical properties of solid matrix and inclusions are then fixed. Based on previous studies on concrete-like materials (Stock et al., 1979), a reference set of mechanical parameters is selected and presented in Table 1.

To effectively showcase the stress–strain response of unit cells to various microstructural elements, we delve into three distinct case: materials comprised entirely of pores, hybrid composites containing both pores and inclusions, and materials reinforced by inclusions. To mitigate the size effect of inclusions and pores, we have maintained a constant total number of inclusions and pores at $N = 300$, with an overall volume fraction of 30%, that is $f + \rho = 30\%$. This approach ensures that inclusions and pores are of comparable size. In this paper, f represents the porosity, and ρ signifies the volume fraction of inclusions. The specifics of Cases 1, 2, and 3 are detailed below.

- Case 1 (purely porous materials): $f = 30\%$, $\rho = 0$;
- Case 2 (mixed composites with pores and inclusions): $f = 15\%$, $\rho = 15\%$;
- Case 3 (inclusion reinforced materials): $f = 0$, $\rho = 30\%$

In Fig. 3, the main results are presented for the porous materials (case 1). Three different loading paths are considered: hydrostatic tension and compression, triaxial compression with different constant confining stresses. It is interesting to notice that due to the presence of pores, there is a failure strength under hydrostatic compression. It means that the failure surface is fully closed on the mean stress axis. In addition, the failure stress under hydrostatic compression (34.37 MPa) is much higher than that under hydrostatic tension (1.76 MPa). The well-known compression-tension dissymmetry property is well captured by the direct numerical simulation. A set of triaxial compression tests with different confining stresses are then simulations. The axial (E_1) and radial (E_3) strains are presented versus the deviatoric stress ($\Sigma_d = \sqrt{\frac{3}{2}\boldsymbol{\Sigma}' : \boldsymbol{\Sigma}'}$, with $\boldsymbol{\Sigma}'$ being the macroscopic deviatoric stress tensor). Three examples are shown in the figure. It is interesting to find that unlike the general idea on geological materials, the failure deviatoric stress does not increase monotonically with the applied confining stress. Indeed, the failure stress for the confining stress of 17 MPa is higher than that of the case with 26 MPa. This can be explained by the fact that due to the effect of pores, the plastic deformation of solid matrix is more important when the confining stress is higher, leading to a decrease of macroscopic failure strength. The stresses at the failure (peak) states are further reported in the classical mean stress ($\Sigma_m = tr\boldsymbol{\Sigma}/3$) versus deviatoric stress plane to represent the numerical failure surface (locus), as shown in the figure. As said above, one gets a closed failure locus along the mean stress axis. Moreover, the failure surface is strongly dissymmetric between the tension and compression. This is consistent with typical experimental results of porous materials (Han et al., 2020; Xie and Shao, 2006, 2012) and with the theoretical predictions of analytical homogenization models (Maghous et al., 2009; Shen et al., 2020).

In Fig. 4, the numerical results are presented for the composite materials containing pores and inclusions at the same scale (Case 2). In this case, the hydrostatic tensile strength (2.51 MPa) is increased with respect to the porous material (Case 1), but it still clearly lower than that of the solid matrix (5 MPa) due to the effect of pores. At the same time, no failure stress is obtained under hydrostatic compression in the range of mean stress considered here. Regarding the triaxial compression loading, four examples of stress–strain curves are presented. As for the porous material above, the failure deviatoric stress first increases and then decreases when the mean stress increases. One obtains a strongly nonlinear failure locus in the Σ_m - Σ_d plane.

In Fig. 5, we show the numerical results for the inclusion reinforced material without pores with $f = 0$, $\rho = 30\%$. For this case, the macroscopic hydrostatic tensile strength (5.02 MPa) is nearly the same as that of the solid matrix (5 MPa). It means that in the absence of pores, the presence of inclusions does not affect the macroscopic tensile strength. This is consistent with the analytical homogenization solution reported in Maghous et al. (2009). However, differently with the linear strength criterion adopted to the solid matrix (cyan line), the macroscopic strength locus is not fully linear, but curved, due to the influence of inclusions, as illustrated by the last graph of the figure.

Based on the representative cases presented above, a high number of numerical simulations (the total number is equal to 1998) are performed in order to construct a large dataset for the establishment of ANN model. For this purpose, different values of porosity f and inclusion fraction ρ are considered here. However, in order to facilitate comparisons, the sum of porosity and inclusion volume fraction is

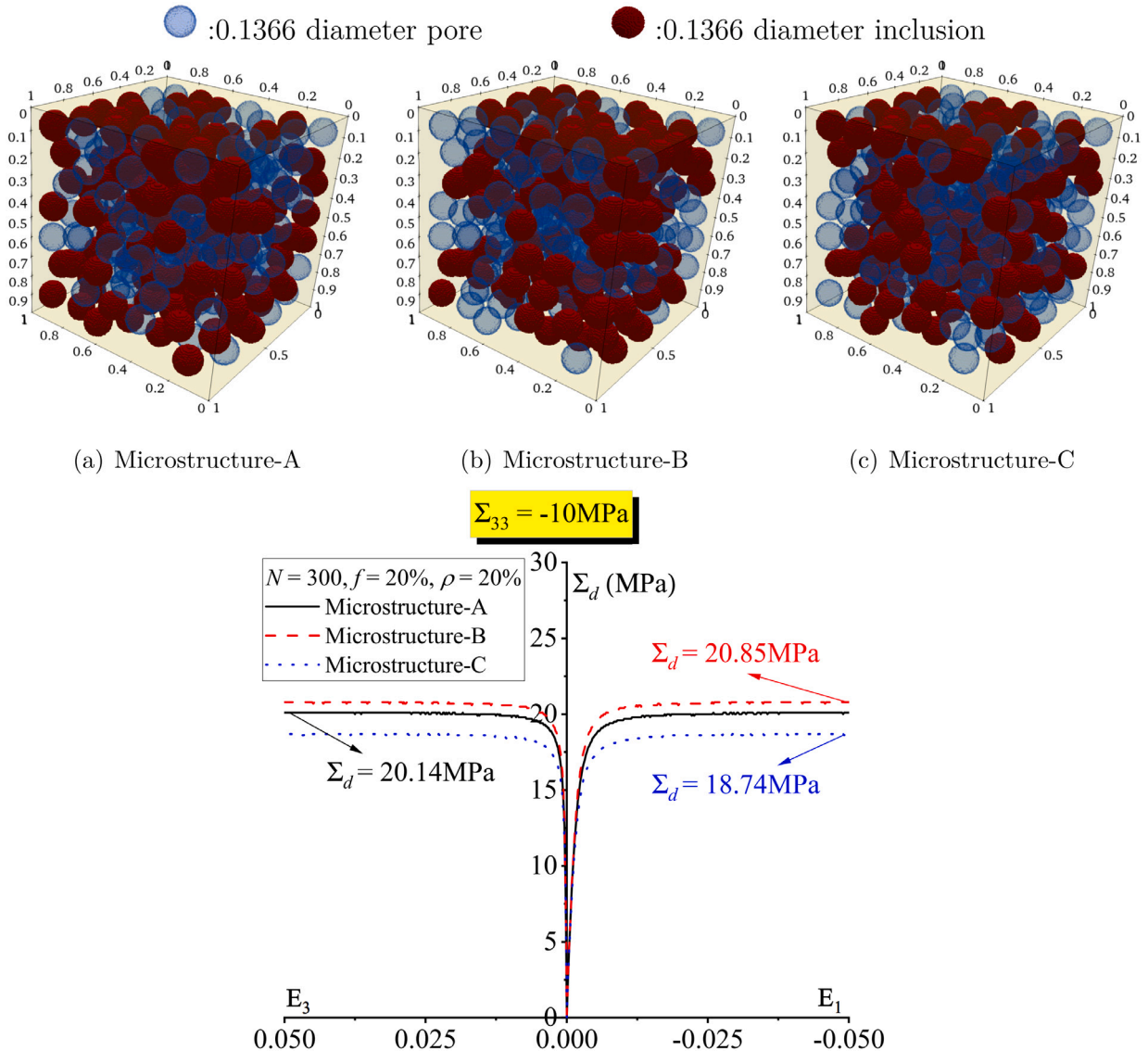

Fig. 2. Effect of spatial location distribution of inclusions and pores on stress–strain cures under $\Sigma_{33} = -10$MPa.

Table 2
The statistics of input and output parameters.

	Σ_m (MPa)	f	ρ	Σ_d (MPa)
Max	5.000	50.000%	50.000%	305.560
Min	−251.853	0.000%	0.000%	0.007
Mean	−86.657	11.551%	14.605%	89.523
Standard deviation	72.965	0.116	0.134	77.841

limited to $f + \rho \leq 50\%$, and the porosity to inclusion ratio takes the following values: $f/\rho \in [0, 1/2, 1/3, 1/4, 1/5, 1, 2, 3, 4, 5, \infty]$. It is worth emphasizing that, according to the parameterization process of the microstructures described above, in this paper, the input values f and ρ in the ANN model uniquely correspond to the microstructures generated by FFT. As a consequence, we collect an original dataset of 1998 sets, each containing Σ_m, f, ρ, and Σ_d. The statistical properties of the dataset are shown in Table 2.

Moreover, correlation analysis is also conducted to capture the interrelationships between the input and output parameters (referred to as features) in the dataset. This statistical measure is highly useful as it describes the degree of correlation among the involved features, reflecting the effectiveness of the dataset in its applicable scope. In this paper, the so-called Pearson correlation coefficient r is employed, and its definition is as follows:

$$r = \frac{\sum_{i=1}^{n}(x_i - \bar{x})(y_i - \bar{y})}{\sqrt{\sum_{i=1}^{n}(x_i - \bar{x})^2}\sqrt{\sum_{i=1}^{n}(y_i - \bar{y})^2}} \tag{2}$$

x and y are two features, while the overline and subscript i respectively represent the mean and the ith observation. The value of r closer to 1 indicates a stronger linear positive correlation between the two features. Conversely, closer to −1 indicates a stronger linear negative correlation. When approaching 0, it indicates no correlation. In this study, the correlation matrices of all input and output features are shown in Fig. 6. From the results of the correlation analysis, we observed a correlation coefficient of −0.59 between porosity and Σ_d, indicating a highly negative correlation between them. Additionally, there is a positive correlation between the volume fraction of inclusions and Σ_d. These findings are consistent with existing patterns, which affirms the validity of the dataset.

2.1. Further analysis of microstructure effect

From the previous results, an interesting phenomenon is observed. It seems that the incorporation of rigid inclusions does not necessarily

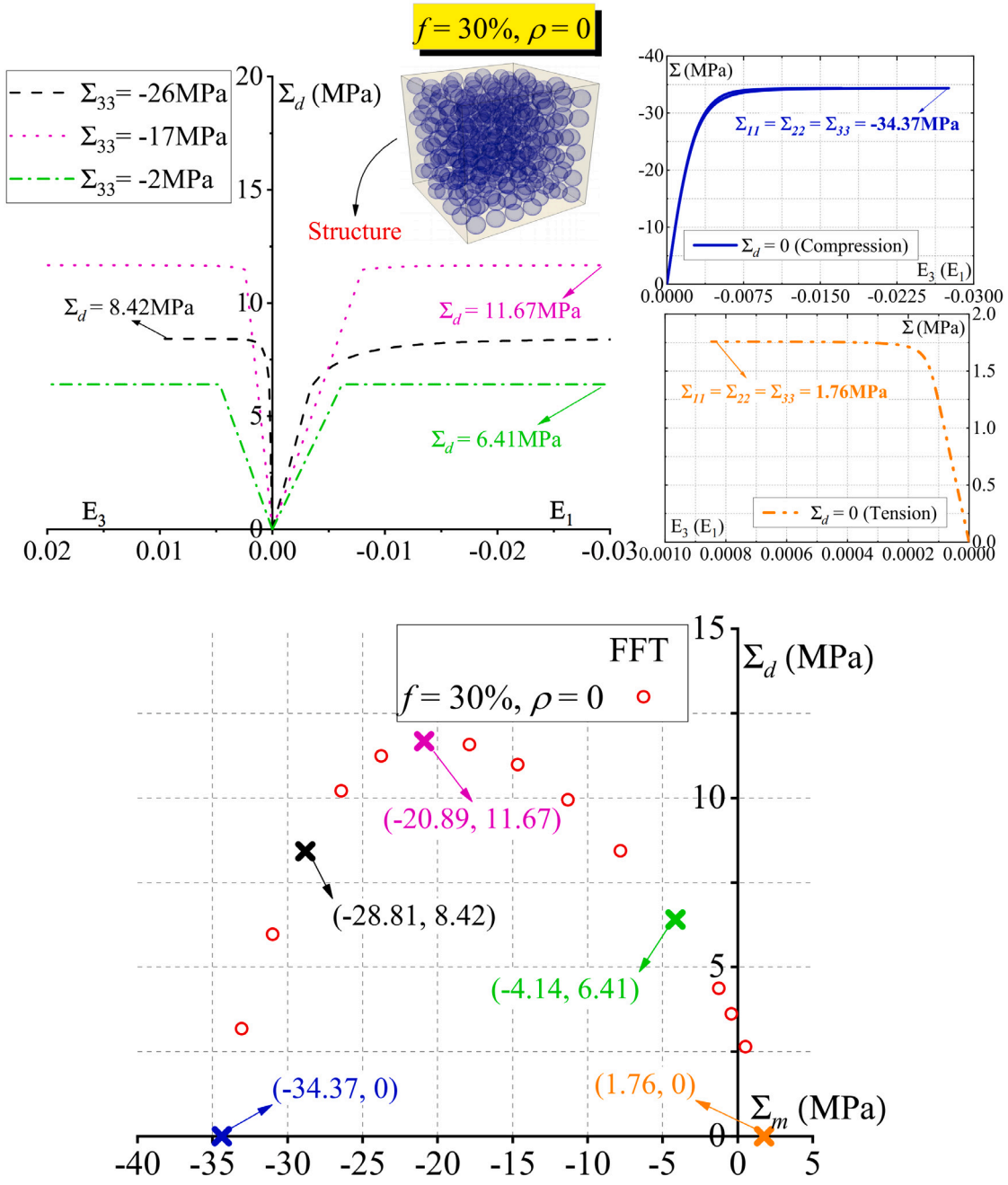

Fig. 3. Stress–strain curves and failure strength locus obtained from DNS for porous material with $f = 30\%$, $\rho = 0$.

lead to a reinforcement of the effective mechanical strength of the material. For instance, as shown above, the strength for the case $f = 20\%$, $\rho = 0$ is higher than that $f = 20\%$, $\rho = 20\%$, especially under high confining stresses. It is worth noticing that in all previous calculations, a fixed total number of spheres ($N = 300$) is chosen to represent pores and inclusions. As a consequence, for a given porosity, the pore size for $f = 20\%$, $\rho = 0$ is smaller than that for $f = 20\%$, $\rho = 20\%$. This would suggest that the failure strength is lower when the pore radius is larger. However, that comparison is not obvious as we compare two basically different microstructures, respectively with and without inclusions. In order to more clearly investigated the relative effects of pores and inclusions as well as their interactions, a complementary set of simulations is here performed. We consider hereby the following three types of microstructures:

(1) Material α: $N = 300$, $f = 20\%$, $\rho = 0$.

(2) Material β: $N = 150$, $f = 20\%$, $\rho = 0$.

(3) Material γ: $N = 300$, $f = 20\%$, $\rho = 20\%$.

The microstructures of three materials are depicted in Fig. 7. The primary difference between Figs. 7(a) and 7(b) lies in the pore size, while that between Figs. 7(b) and 7(c) is the presence of inclusions.

In Fig. 8, one illustrates the strength surfaces of three materials. By comparing the cases α and β, we can see that the strength surface of the material α is located below that of β. This should indicate that as the pore size increases, the macroscopic strength becomes higher. A quantitative comparison is given for a triaxial compression test with 40 MPa confining stress. However the strength difference between these two materials is very small. One can conclude that at the material scale considered here, the pore size has a relatively minor impact on the material macroscopic strength. Comparing now the material γ with the previous two ones, say α and β. It is observed that for low values of mean stress, say less than 25 MPa, the deviatoric stress at failure of γ is higher than those of α and β. A quantitative comparison is given for the

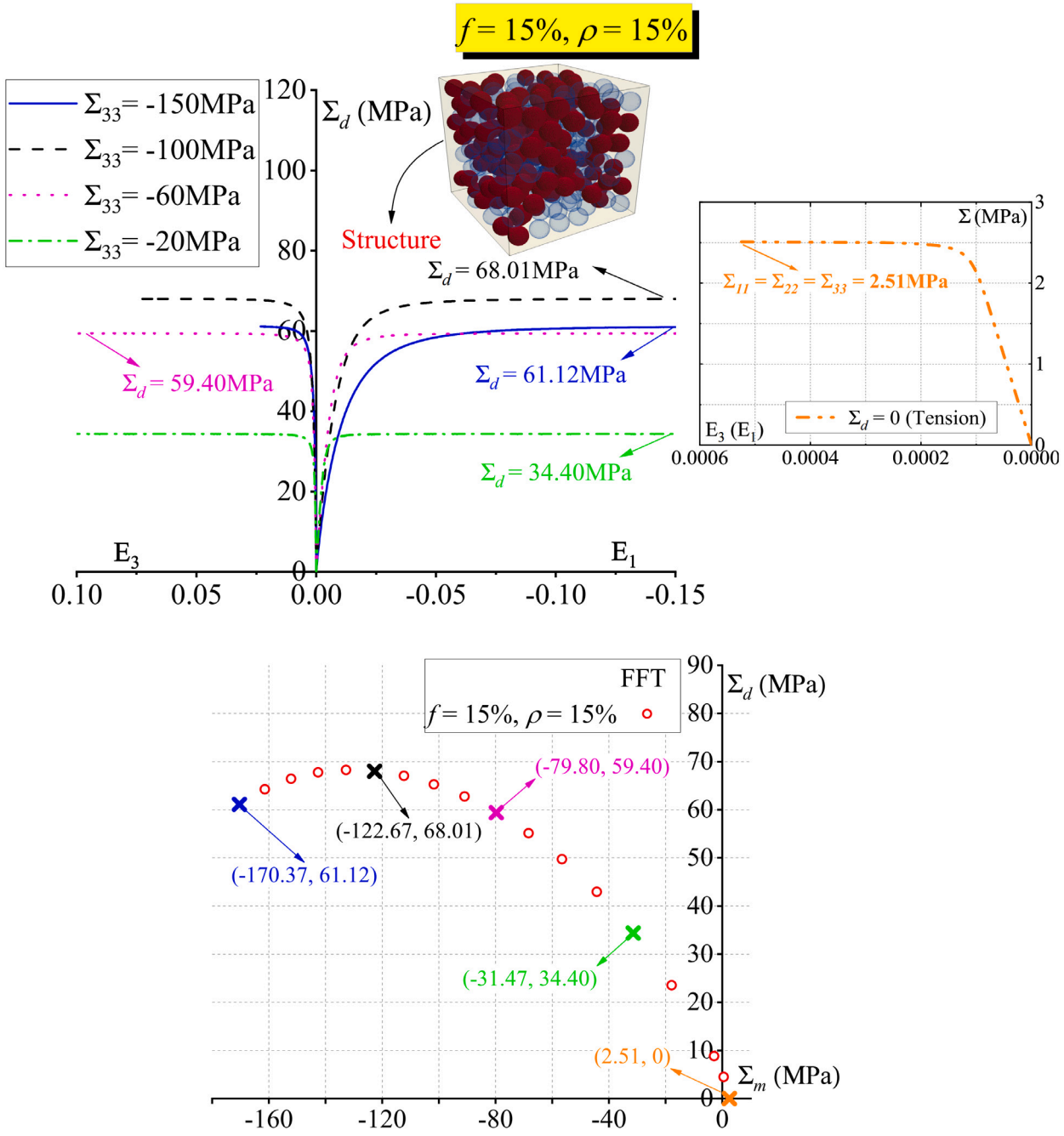

Fig. 4. Stress–strain curves and failure strength locus obtained from DNS for the composite materials with f = 15% and ρ = 15%.

case of triaxial compression test with 5 MPa confining stress. However, when the mean stress becomes higher, there is a significant decrease of deviatoric strength for the material γ, which is lower than those of the two materials without the presence of inclusions. This clearly confirms that the presence of inclusions enhances the materials failure strength under low mean stress but has a weakening effect under high mean stress.

In order to better understand the origin of difference between three materials, the full stress–strain curves during two triaxial compression tests respectively with $\Sigma_{33} = -5$ MPa and $\Sigma_{33} = -40$ MPa are shown in Fig. 9. It is seen that very small differences of deformation are observed between the materials α and β. Under $\Sigma_{33} = -5$ MPa, the material γ exhibits a more important plastic hardening process, leading to a higher peak strength than the other two materials. Inversely, for the case with $\Sigma_{33} = -40$ MPa, the material γ has a very small macroscopic plastic yield stress, resulting in a faster plastic deformation kinetics and a lower peak strength than two other materials.

To further elucidate the reasons behind the significant impact observed on material γ under conditions of elevated mean stress, it is essential to examine the synergy between the microstructural constituents of the material and the stress applied to it. Under scenarios of heightened mean stress, the presence of inclusions, imperfections, and grain boundaries within the microstructure becomes instrumental in the initiation and propagation of cracks. These microstructural elements act as stress amplifiers, facilitating the onset and development of cracks even under relatively low levels of applied stress. As mean stress intensifies, the probability of crack initiation and propagation escalates, exacerbated by the augmented effects of stress concentration inherent within the microstructure. Moreover, inclusions present within

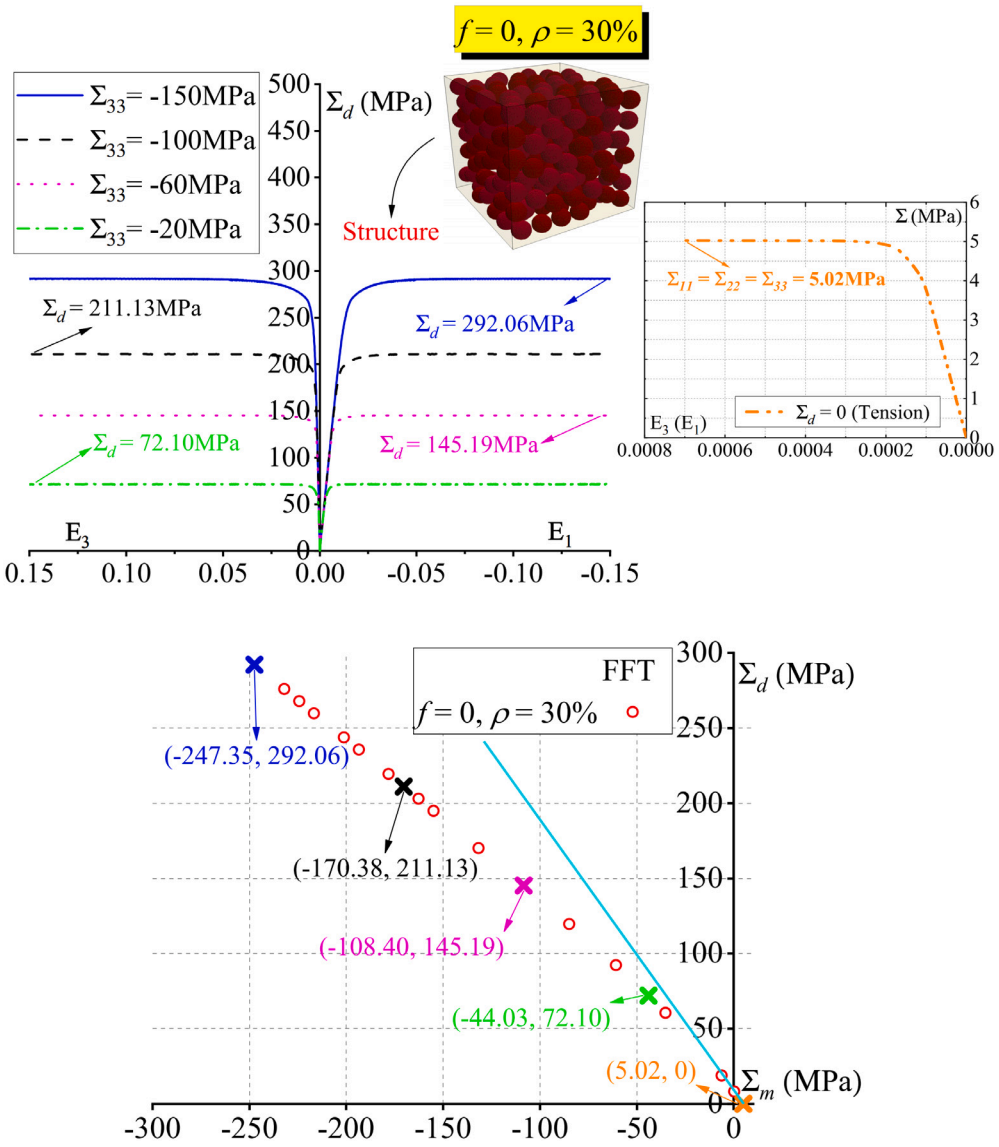

Fig. 5. Stress–strain curves and failure strength locus obtained from DNS for the inclusion reinforced material with $f = 0$ and $\rho = 30\%$.

the material can serve as preferential locations for crack initiation, particularly under conditions where the mean stress exceeds the resilience of the inclusion–matrix interface. This leads to expedited crack growth, thereby significantly undermining the material's structural integrity. In the forthcoming stages of our research, we will seek to validate these observations through experimental studies employing 3D printing technology, with a specific focus on the role of inclusions and their effect on the mechanical properties of materials. These empirical validations are expected to significantly enhance our understanding of the importance of precisely modeling inclusions in the analytical assessment of Material γ, thereby contributing valuable insights to the domain.

3. Construction of ANN-based model

3.1. Principle of artificial neural network

Artificial neural network (ANN) is one of the most popularly used statistical models to determine input–output relationships through a series of interconnected data structures with multiple neurons that have the ability to perform a large number of calculations for data processing and information representation (Lawal et al., 2021; Adesanya et al., 2021). An ANN model can be trained to predict the desired output from a given input. The ability of ANN structures to process information depends on the weights connecting the neurons (Jain et al., 1996). The most widely used feed forward neural network with a back propagation (BP) algorithm is adopted in this study. The structure of a typical feed-forward neural network consists of an input layer and an output layer and at least one hidden layer, and each layer has a number of neurons. The number of neurons in the input and output layers is determined according to the problem under study. The number of hidden layers and the number of neurons per layer are very important for the accuracy of the model, and they are the hyperparameters that need to be tuned. Moreover, the neurons are massively interconnected and improve their predictive capability as the network evolves (Chung and Abbott, 2021). Additionally, each neuron performs two tasks: the summation and activation. The structure of a neuron is shown in Fig. 10. The lth layer has n neurons while the $(l-1)$th layer has m neurons. The input/output relationship of a neuron is indicated in a matrix form as follows:

$$a_i^l = \sigma\left(\sum_{j=1}^{m} \boldsymbol{w}_{ij}^l \boldsymbol{a}_j^{l-1} + \boldsymbol{b}_i^l\right) \tag{3}$$

where $\boldsymbol{w}_{ij}^l$ is the weight matrix from the $(l-1)$th layer to the lth layer, $\boldsymbol{b}_i^l$ is the bias vector for inputs on the lth layer, The indices $i = 1, 2, \ldots, n$,

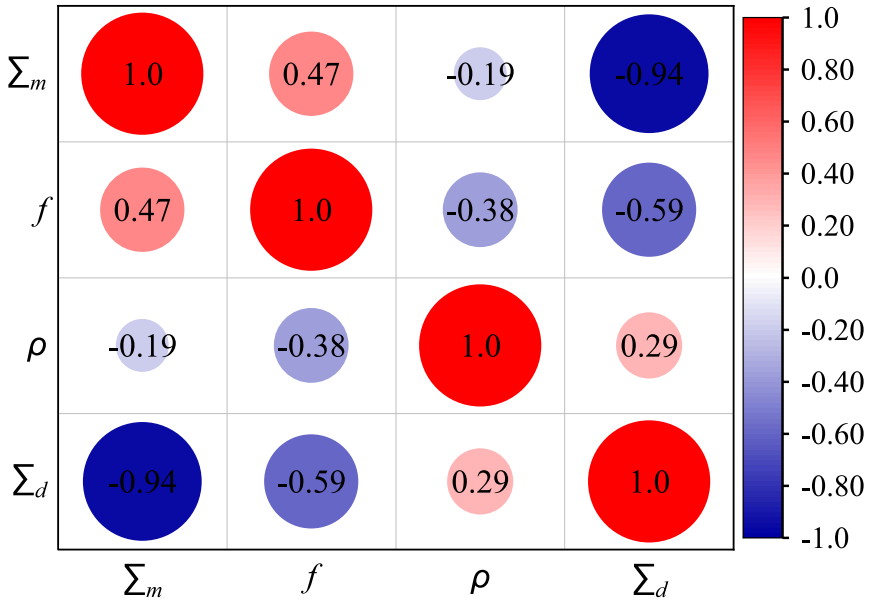

Fig. 6. Correlation matrix of features in original dataset.

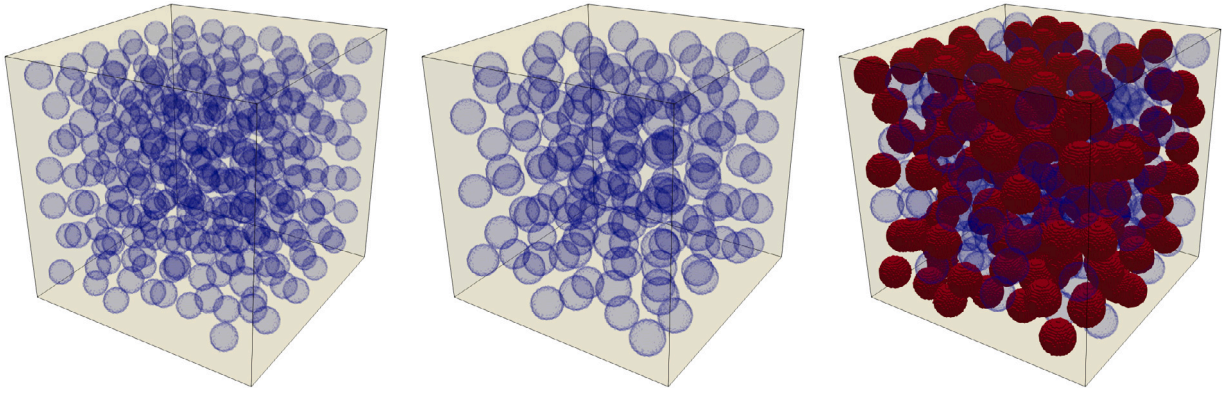

(a) $N = 300,\ f = 20\%,\ \rho = 0$ (b) $N = 150,\ f = 20\%,\ \rho = 0$ (c) $N = 300,\ f = 20\%,\ \rho = 20\%$

Fig. 7. Microstructure of the three materials studied.

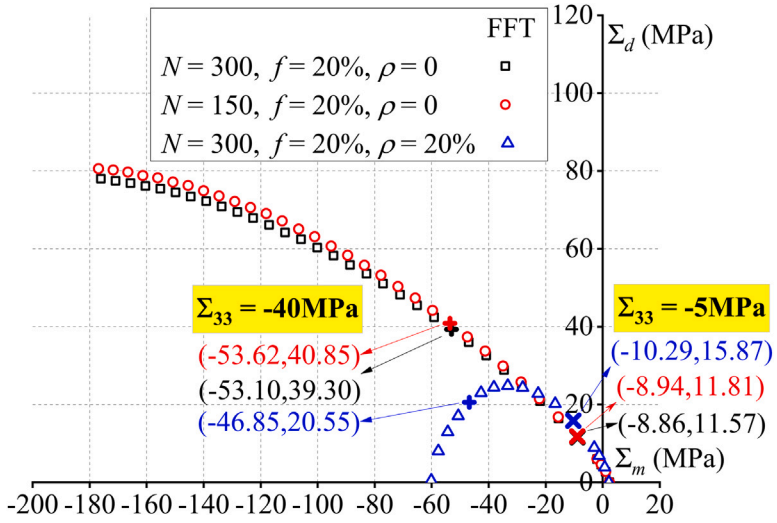

Fig. 8. Comparison of macroscopic strength surfaces of three materials.

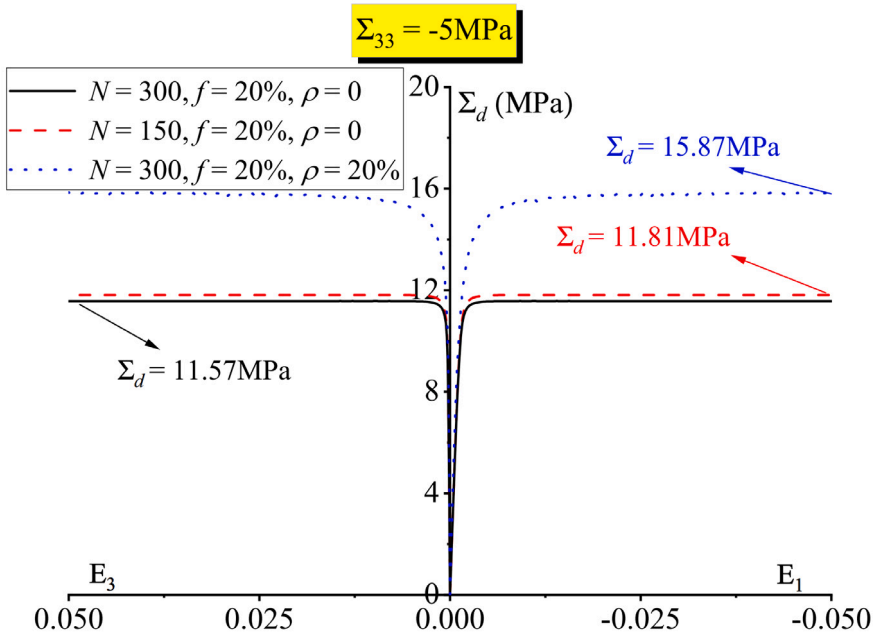

(a) Σ_{33} = -5MPa

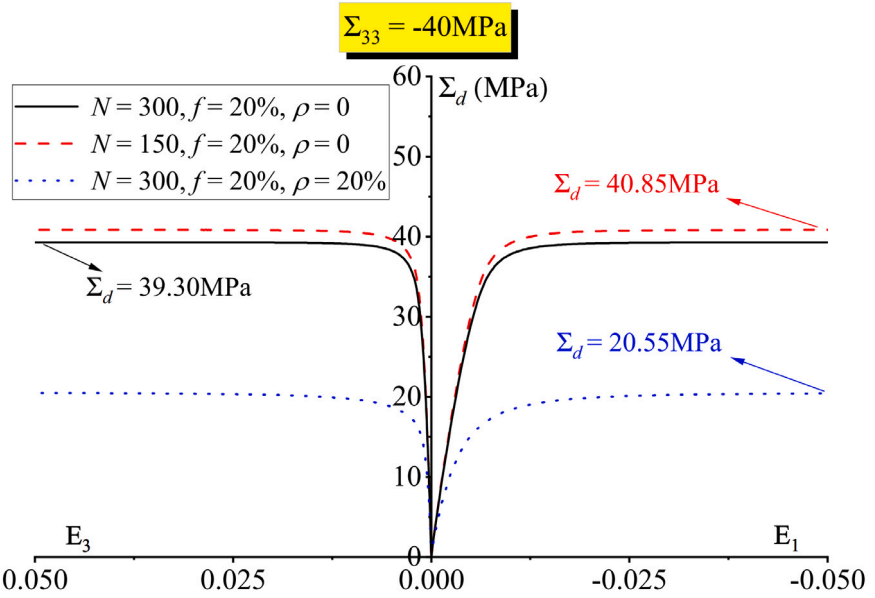

(b) Σ_{33} = -40MPa

Fig. 9. Stress–strain curves of three materials in two triaxial compression tests with different confining stresses.

and $j = 1, 2, \ldots, m$. σ represents the activation function. In this paper, ReLU ($\sigma(x) = max(0, x)$) is used as the activation function, except for the output node where $\sigma(x) = x$ is used.

The fitting ability of the neural network is determined by its weights and bias. By comparing the network's outputs with the target outputs, the weights and bias are adjusted. The objective is to lower the value of the loss function until the network output closely resembles the target with a respectable degree of accuracy. Network training or learning is the process of adjusting the weights. The loss function used in this study is mean squared error (MSE). The mean absolute error (MAE) is applied during validation. In addition, the model's parameters are automatically adjusted using the error back propagation and weight updating mechanisms to increase accuracy, and the Adam function is adopted to accelerate the convergence of the model.

3.2. Preprocessing of original dataset

The original dataset has to be preprocessed before building an ANN model, the purpose is to make the model more accurate and robust (Qazi et al., 2015). The two parts of dataset preprocessing are the reasonable division of the original dataset and the normalization of the input data. Normalization is to reduce the impact of input data with different scales on the accuracy of the model. In this study, the original dataset (1998 sets) is divided into three subsets: training dataset (1198 sets), validation dataset (400 sets), and test dataset (400 sets). And

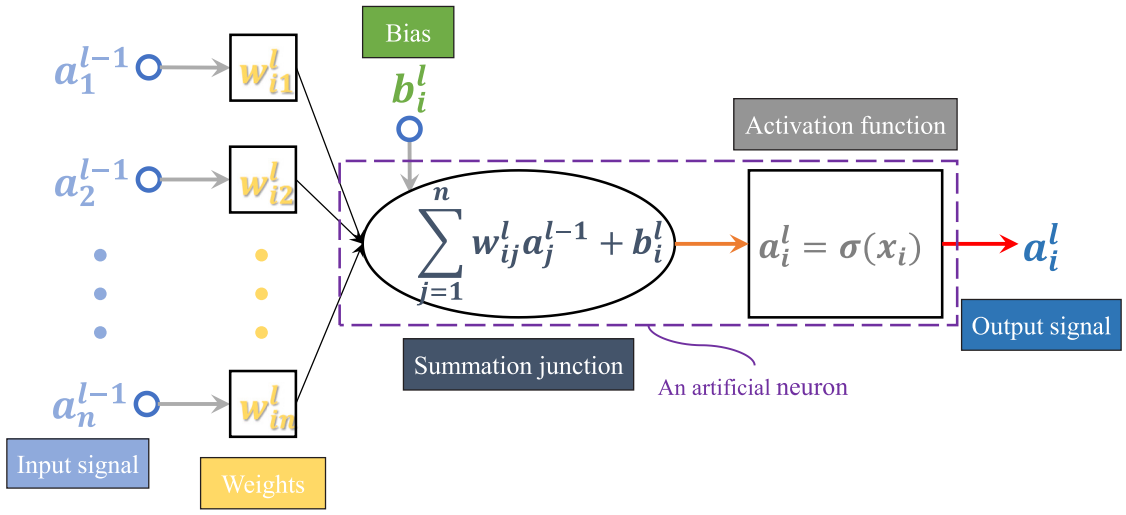

Fig. 10. Illustration of neuronal structure.

Table 3
Mean $\bar{k}$ and standard deviation σ of input data.

	Σ_m (MPa)	f	ρ
$\bar{k}$	−86.265	11.671%	14.562%
σ	73.022	0.117	0.133

Table 4
Ideal value of different statistical parameters.

Parameters	APE	MAPE	RMSE	RSR	WMAPE	R^2
Ideal value	0	0	0	0	0	1

normalize all input data according to the Eq. (4). (the output data does not require any processing). For more detailed information about this section, the reader is referred to Xue et al. (2021).

$$x_i = \frac{k_i - \bar{k}}{\sigma} \tag{4}$$

where k_i, x_i, $\bar{k}$, σ are the actual value of the data, the normalized value, the mean and standard deviation in the data samples, respectively. In this paper, the mean and standard deviation of the input data are shown in Table 3.

3.3. Performance evaluation

In order to quantitatively evaluate the predictive performance of the ANN model, seven different statistical parameters are adopted: absolute percentage error (APE), mean absolute percentage error (MAPE), root mean square error (RMSE), root mean square error to observation's standard deviation ratio (RSR) and weighted mean absolute percentage error (WMAPE), coefficient of determination (R^2) (Asteris et al., 2021; Duan et al., 2021; Armaghani et al., 2017; Chen et al., 2019; Hajihassani et al., 2019; Yang et al., 2019). The mathematical formulations of which are given by:

$$APE = \sum_{i=1}^{n} \left| \frac{y_i - \hat{y}_i}{y_i} \right| \times 100\% \tag{5}$$

$$MAPE = \frac{1}{n} \sum_{i=1}^{n} \left| \frac{y_i - \hat{y}_i}{y_i} \right| \times 100\% \tag{6}$$

$$RMSE = \sqrt{\frac{1}{n} \sum_{i=1}^{n} (y_i - \hat{y}_i)^2} \tag{7}$$

$$RSR = \frac{RMSE}{\sqrt{\frac{1}{n} \sum_{i=1}^{n} (y_i - \bar{y})^2}} \tag{8}$$

$$WMAPE = \frac{\sum_{i=1}^{n} \left| \frac{y_i - \hat{y}_i}{y_i} \right| \times y_i}{\sum_{i=1}^{n} y_i} \tag{9}$$

$$R^2 = 1 - \frac{\sum_{i=1}^{n} (y_i - \hat{y}_i)^2}{\sum_{i=1}^{n} (\bar{y} - \hat{y}_i)^2} \tag{10}$$

in which $\bar{y} = \frac{\sum_{i=1}^{n} y_i}{n}$, y_i is ith actual value, $\hat{y}_i$ is ith calculated output values. In theory, R^2 value ranges from 0 to 1 while the model has the healthy predictive ability when it is near to 1 and is not analyzing whatever when it is near to 0. These performance metrics are a good measure of the overall predictive accuracy. For a perfect predictive model, the values of these indices should be equal to their ideal value, the details of which are presented in Table 4.

Furthermore, a following new engineering index, the a^{20}-$index$, has been recently proposed for the reliability assessment of ANN models (Apostolopoulou et al., 2019; Asteris et al., 2019; Huang et al., 2019; Asteris et al., 2021).

$$a^{20}\text{-}index = \frac{m^{20}}{M} \tag{11}$$

where M is the number of dataset sample and m^{20} is the number of samples with value of ratio of actual and predicted value between 0.80 and 1.20. Note that, for a perfect predictive model, the value of a^{20}-$index$ is expected to be unity. The proposed a^{20}-$index$ has the advantage that its value has a physical engineering meaning. It declares the number of the samples that satisfies the predicted values with a deviation ±20% compared to actual values.

3.4. Structure and algorithm of a specific model

In this study, the ANN model is trained using the advanced open source Keras (Gulli and Pal, 2017) library on the TensorFlow (Shukla and Fricklas, 2018) framework. Fig. 11 illustrates the process for building an ANN model for predicting the strength surface of concrete-like materials. There are two main phases. (1) Preprocessing of the original dataset obtained using the FFT-based numerical simulation method. The inputs to the model are Σ_m, f and ρ, and the output is Σ_d. The train dataset, validation dataset, and test dataset are 1198, 400, and 400 sets, respectively. (2) Determining the optimal hyperparameters of the model. The hyperparameters of ANN model include the number of hidden layers, the number of neurons in each layer, the activation function, the loss function, etc. Hyperparameters are very important to the accuracy of the model. Unfortunately, there is no guidance on choosing the optimal hyperparameters. In the present work, inspired by previous studies on similar problems (Lee, 2003; Liu et al., 2021;

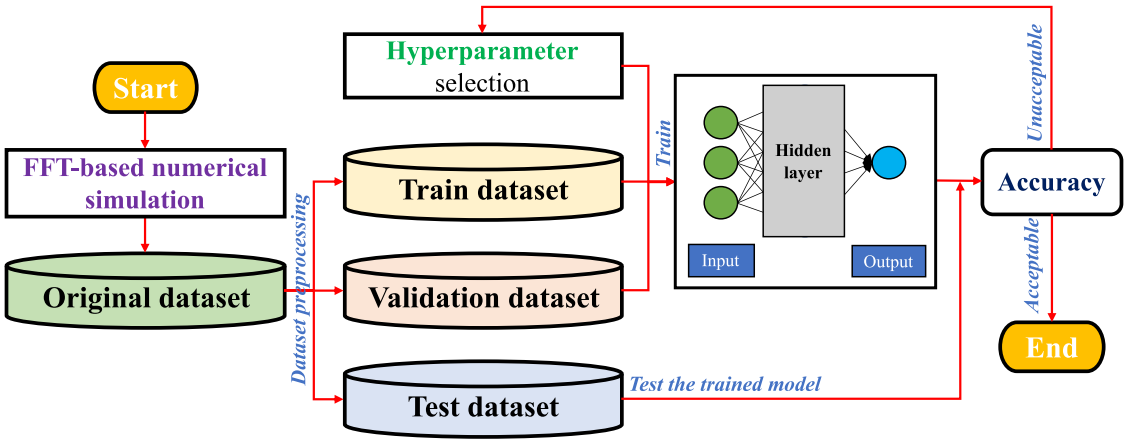

Fig. 11. Flowchart for building an ANN-based model.

Table 5
Hyper-parameters of the ANN model for predicting the macroscopic strength surface of concrete-like materials.

Input layer	Hidden layer	Output layer	Loss function	Optimizer
Σ_m, f, ρ	2 × 100×ReLU	Σ_d	MSE	Adam

Table 6
Details of performance indices of ANN model in train, validation and test sets.

Dataset type	MAPE	RMSE	RSR	WMAPE	R^2	a^{20}-$index$
Train	4.07585%	0.27446	0.00353	0.00210	0.99999	98.08013%
Validation	5.23597%	0.71933	0.00913	0.00381	0.99992	96.00000%
Test	4.93063%	0.45124	0.00584	0.00324	0.99997	97.25000%

Congro et al., 2021; Tam et al., 2022), several combinations of hyper-parameters were obtained and a trial-and-error approach was used to select the structure of the model. To be more precise, the initial model hyperparameters are employed first, followed by model training and evaluation using the training and validation dataset and test dataset, respectively, to compare the accuracy of various models and select the optimal hyperparameters. If the accuracy of the model does not meet the requirements, the hyperparameters are selected again until the accuracy requirements are satisfied. After our experimentation, a BP neural network with two hidden layers and 100 neurons in each is constructed. The network structure is shown in Fig. 12. The input/output and hyperparameters are presented in Table 5. The MSE is used as the loss function and the Adam is adopted as the optimizer. The training and validation processes are illustrated in terms of the MAE. Further, the Batch-size is 32 and maximum number of epochs is 1000 for training.

3.5. Performance of model

In this subsection, the established ANN model is comprehensively evaluated based on mathematical statistics. Fig. 13 shows the evolution of the MAE and loss function for the training and validation sets during the training phase. It can be seen that the convergence of the model is very fast, and both the loss function and MAE drop to the minimum value very quickly. After 1000 epochs, the final values of MAE and loss function are 0.23697, 0.11124 for the training dataset and 0.34972, 0.51743 for the validation one. There is the relatively small difference for model performance in the train and validation sets, which also indicates that the model is not over-fitting.

In order to further elaborate the accuracy of the model, the performance of the model is verified on the train, validation and test datasets, respectively. The comparison between the actual and predicted values of the ANN model are shown in Fig. 14. The actual values of the three datasets and their predicted ones are distributed on the $\Sigma_d = \Sigma_d'$ line, which denotes the high accuracy of the ANN model. It is worth noting that there is no significant difference in the performance of the model between these three types of datasets.

Furthermore, Table 6 represents the details of the performance parameters of the ANN model. As can be seen, the model achieves over 99% accuracy in the train (R^2 = 0.99999), validation (R^2 = 0.99992) and test (R^2 = 0.99997) dataset. And the values of RMSE (training = 0.27446, validation = 0.71933 and testing = 0.45124) indicate the acceptable precision. The ANN also showed excellent training results in terms of MAPE, RSR and WMAPE. Physically meaningful performance indices (a^{20}-$index$ = 98.08013% in the train dataset, a^{20}-$index$ = 97.25000% in the test dataset) shows the generalization capability of the model in both datasets. In addition, a model with high prediction accuracy during the test dataset is generally considered a robust model (Asteris et al., 2021). From the performance indices of different datasets types on the model, the train dataset has the best predictions, followed by the test dataset, while the validation dataset has the worst results, and the performance of test dataset and the train dataset are also very close to each other. It shows that the trained model is not only accurate, but also robust.

3.6. Limitations and error sources

To investigate the limitations and error sources of the ANN model, the error distribution of the model was first analyzed. Unless otherwise noted, errors in this section refer to absolute percentage error (APE). Fig. 15 shows the cumulative curves with errors less than 10% for the three types of datasets. It can be observed that about 95% of the datasets have an error of less than 10% and their MAPE is about 4.75%, which are good indicators of the accuracy of the model. For this study, model errors within 10% are acceptable, so this piece of the model error sources will not be considered further. The focus of this section is to investigate the situation when the error of the model is greater than 10%. There are 94 datasets (from train, test and validation datasets) with an error over 10%, accounting for 4.70% of the total dataset (94/1998 ≈ 4.70%). Fig. 16 illustrates the corresponding inputs and outputs for these datasets, where Open represents the open form of the complete strength surface for the corresponding material, while Closed is its closed form. Various combinations of f and ρ represent different types of materials. It can be noted that the strength surface form is closed for most materials (the proportion is 75/94 ≈ 79.79%) and the corresponding Σ_d values are between 0 and 5 MPa. The reason for this error is that this closed strength surface data is underrepresented in the dataset where the model was trained. In fact, this is mainly limited by the material under study. For a material like concrete, it has a

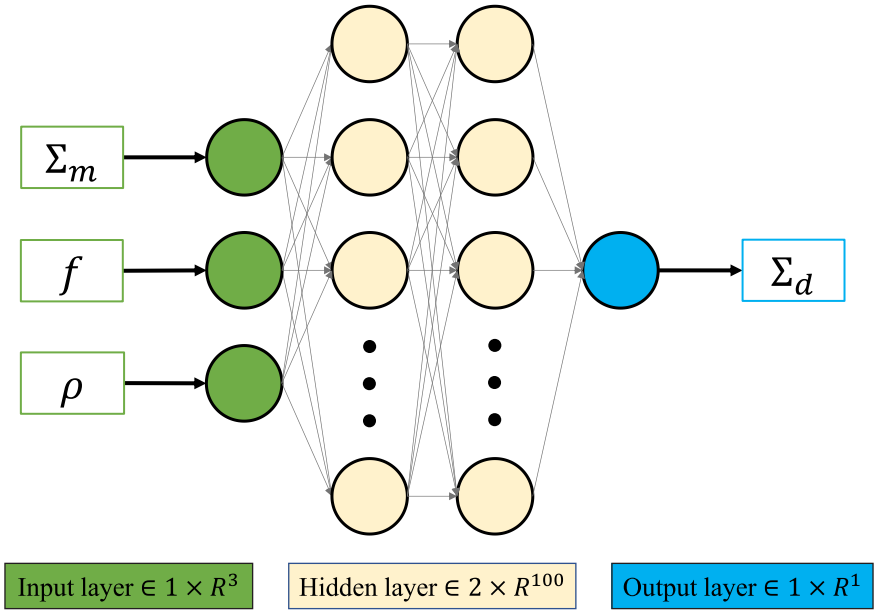

Fig. 12. Established BP neural network model for failure strength prediction.

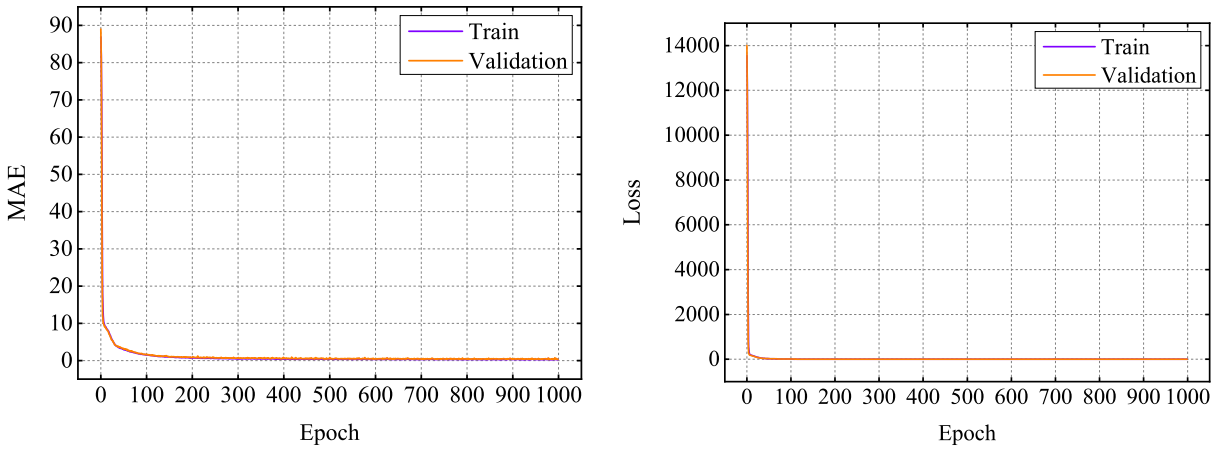

Fig. 13. MAE and loss function evolution during training process.

large strength and most of the strength surfaces are open. Therefore, the number of datasets collected for closed strength surfaces is less, which also leads to a shortage of training for the model in this range, so the accuracy is bad. For materials with open strength surfaces, the inaccuracy of model predictions is concentrated in the case of relatively small Σ_m. In fact, this is due to the low tensile strength of the concrete-like material and the limiting value of the confining pressure, in which case the number of datasets used to train the model is also relatively small, so the error of the model is large at this stage.

At present, an effective way to improve the accuracy of ANN models within a specified input interval is to appropriately increase the input and output data for that interval, add them to the original dataset, and then retrain the model (Burke et al., 1997; Santos et al., 2021). However, it is considered unnecessary in the present study. The purpose of this paper is to obtain the macroscopic strength surface of a material. As can be seen in Fig. 16, the ANN model is inaccurate at only one or a few points, which actually has less effect on the overall strength surface of the material. From the model performance indices presented previously, it can be believed that the current ANN model is valid and accurate.

4. Application to failure strength prediction

4.1. Methodology

The purpose of this study is to determine the strength locus of a heterogeneous material by using the developed ANN model. For this purpose, it is useful to first define the general frame of application.

The methodology adopted is as follows. The microstructure of material is characterized by the porosity f and the inclusion volume fraction ρ. In practice, can be measured by various techniques such as mercury intrusion porosimetry (MIP), nuclear magnetic resonance (NMR), and X-ray Diffraction (XRD). Then, for a given value of mean stress Σ_m, the corresponding value of deviatoric stress at failure should

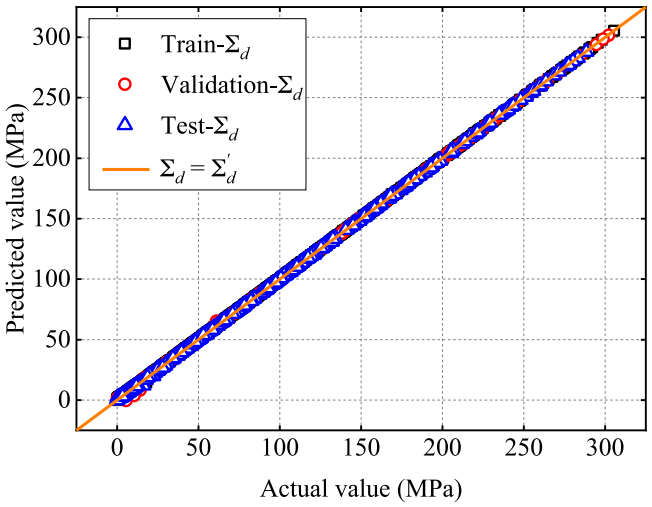

Fig. 14. Correlation between predicted and actual values of Σ_d for train, validation and test sets.

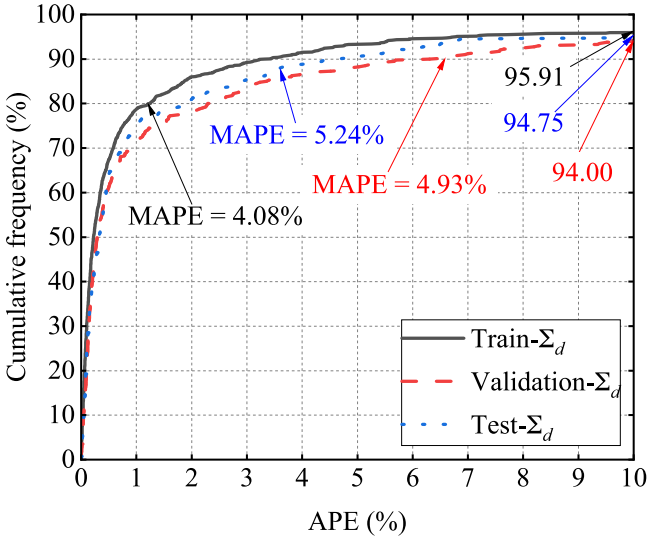

Fig. 15. Cumulative frequency versus the absolute percentage error (APE) for the ANN model.

be predicted by the proposed ANN model. Therefore, it is needed to first select the representative range of mean stress Σ_m. Its maximum value is the hydrostatic failure stress denoted as Σ_m^t, which can be obtained from the FFT-based direct numerical simulation for a given set of f and ρ. The minimum (algebra) value of mean stress is the hydrostatic strength Σ_m^c, which can be also obtained from the FFT-based direct numerical. However, for some cases such as the inclusion reinforced material discussed above, the value of Σ_m^c can be very large or does not exist (the failure locus is not closed). Therefore, for the sake of convenience, the minimum value of mean stress is here fixed to −150 MPa.

In order to illustrate this procedure, an example is here presented in detail. We consider a porous material with $f = 25\%$ and $\rho = 0$. The mechanical parameters are the same as those used in the FTT based simulations (see Table 1). In Table 7, one shows a selection of 12 stress state ta failure. The value of mean stress Σ_m is bounded by its hydrostatic tensile strength (2.03 MPa) and compression strength (−83.25 MPa). At these two particular states, the corresponding deviatoric stresses are equal to zero. Between these two bounds, for each value of mean stress Σ_m, the corresponding value of deviatoric stress Σ_d

Table 7
An example of input values (f, ρ, Σ_m) and output result (Σ_d) for a porous material with $f = 25\%$ and $\rho = 0$.

Number	f	ρ	Σ_m (MPa)	Σ_d (MPa)
1	25%	0	**−83.25**	**0.00**
2	25%	0	−78.23	9.68
3	25%	0	−70.83	17.50
4	25%	0	−62.57	22.70
5	25%	0	−53.23	24.70
6	25%	0	−43.10	24.30
7	25%	0	−32.23	21.70
8	25%	0	−20.70	17.10
9	25%	0	−8.40	10.20
10	25%	0	−0.32	3.95
11	25%	0	1.38	1.85
12	25%	0	**2.03**	**0.00**

Bolded values are obtained from FTT DNS.

at failure is predicted by the ANN model. Based on these results, the strength locus of the considered porous material is drawn and presented in Fig. 17.

4.2. Results and discussions

The proposed ANN model is now applied to predicting the failure stresses of three representative groups of materials defined above. The input mechanical parameters are the same as those used in the direct numerical simulations. Moreover, the results of the FFT simulations are taken as the reference solutions for the validation of the ANN model. In addition, for convenience, the values of Σ_m and Σ_d are normalized as Σ_m/Th and Σ_d/Th, with $Th = 4.5$ MPa.

In the first group (Case 1), porous materials without inclusions (ρ: $f = 0$) are studied, while in the third group (Case 3) composites reinforced by inclusions without pores (ρ: $f = \infty$) are investigated. In Fig. 18, one shows the strength locus of these two types of materials with different values of porosity or inclusion volume fraction. It is first seen that there is a very good concordance between the failure stresses predicted by the ANN model and those from the direct FFT simulations. This illustrates the good accuracy of the ANN model. Moreover, for the porous materials, the mechanical strength is strongly affected by porosity. The failure surface gradually shifts downward with the increase of porosity f, and the strength surface becomes closed along the mean stress axis when the porosity value is high enough, for instance $f \geq 25\%$ for the present case. For the inclusion reinforced materials, the mechanical strength gradually increases as the volume fraction of inclusions ρ is higher. However, the strengthening effect due to inclusions is very limited. Therefore, although the mechanical failure strength of heterogeneous materials is affected by pores and inclusions, but the impact of pores is generally much more significant than that of inclusions. Similar results have been presented by some previous experimental studies Murakami and Endo (1994), Cao et al. (2021), Chawla et al. (2021).

The second group covers a wide range of composite materials containing pores and inclusions at the same scale. For convenience, three sub-cases are separated. In the first sub-case, the material contains a same volume fraction of inclusions and pores (ρ: f = 1:1). The corresponding results are shown in Fig. 19. Again, the predictions of the ANN model are quasi identical to the reference results provided by the FFT simulations. Similarly to the porous materials presented above, as the values of ρ and f increase, the strength surface of the material shifts downward and becomes closed when $\rho = f \geq 20\%$. This result indicates that in spite of the increase of inclusion volume fraction, the mechanical strength of materials still decreases if the porosity becomes higher. That clearly confirms the dominating role of porosity with respect to the inclusion volume fraction. The reason for this phenomenon is that the plastic yielding of material generally tends to occur in the weak zones. Indeed, the presence of pores facilitates the plastic yielding of

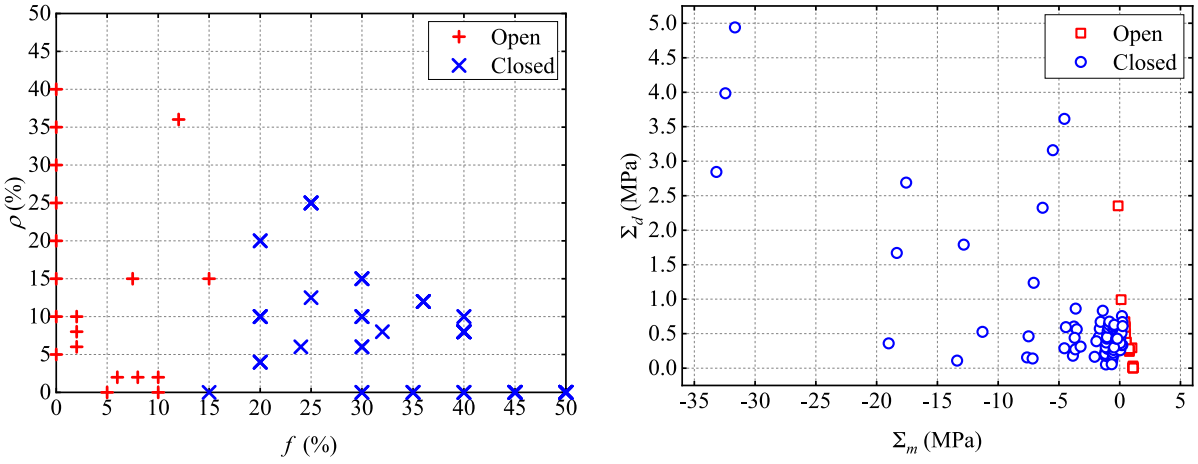

Fig. 16. Input and output distributions for datasets with errors greater than 10%, where Open represents the open form of the complete strength surface for the corresponding material, while Closed indicates its closed form.

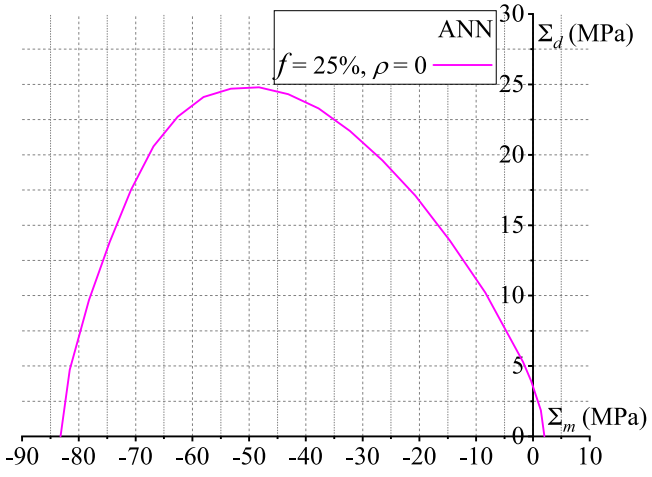

Fig. 17. Macroscopic strength locus predicted by the ANN model for $f = 25\%$, $\rho = 0$.

solid matrix at the microscopic scale while the strengthening effect of inclusions is moderate.

In the second sub-case, one considers materials with more pores than inclusions, respectively with ρ: f = 1:2 and ρ: f = 1:3. The corresponding failure stress surfaces are displayed in Fig. 20. Once more, the comparisons with the results of FFT simulations confirm the high accuracy of the ANN model. The general trend of failure surface is very similar to that of porous materials. The macroscopic failure strength is dominantly controlled by the porosity. The dominating role of porosity is even more significant when the ratio ρ: f is lower, as shown in Fig. 20(b).

In the last sub-case, we consider those materials with more inclusions than pores. Three different ratios are used here such as ρ: f = 2:1, ρ: f = 3:1 and ρ: f = 5:1. The results obtained are shown in Fig. 21. Like the previous cases, the predictions of the ANN model are again confirmed to be accurate with respect ot the reference results of the FFT simulations. About the evolution of macroscopic strength surface, there is clearly a strong competition between weakening impact by pores and strengthening effect by inclusions. When the ρ: f is relatively low, for example ρ: f = 2:1, the strength surface of the material is still mainly controlled by the porosity although an important presence of inclusions. More precisely, the failure stresses decrease with the increase of porosity and inclusion fraction. But for higher inclusion-porosity ratios, for instance ρ: f = 3:1 and ρ: f = 5:1, the weakening effect of porosity becomes more and more attenuated. One obtains an open strength surface in the mean stress axis for all cases studied. Moreover, another interesting phenomenon is observed for this category of materials. It seems that for those materials with a high volume fraction of inclusions, the effect of porosity is no more systematical and depends on the value of main stress. Taking the case with ρ: f = 5:1, an simultaneous increase of porosity and inclusion fraction has a weakening effect for high values of mean stress but a strengthening consequence for low mean stresses. This phenomenon is more visible when the ratio ρ: f is higher. It means that due to interaction between pores and inclusions, the plastic deformation in the domain of low mean stresses is attenuated by an strong presence of inclusions.

In order to investigate the respective effects of pores and inclusions on the macroscopic failure strength, it is interesting to compare the results reported in Fig. 18(a) and Fig. 19. More specifically, one compares the materials respectively with f = 15%, ρ = 0 and f = 15%, ρ = 15%, as well as f = 20%, ρ = 0 and f = 20%, ρ = 20%. In each of these two sets, the porosity remains unchanged while the inclusion fraction is changed. The comparisons of strength surface for two sets are presented in Fig. 22. As the accuracy of the ANN model is already clearly demonstrated in all previous cases, only the predicted results of the ANN model are reported here. First, for two values of porosity considered here, in the absence of inclusion (ρ = 0), the failure surfaces are not closed. The failure strength is lower for f = 20% than for f = 15 and the related failure surface is more curved toward the mean stress axis. The weakening effect of pores alone is clearly confirmed. However, by adding inclusions into materials, one obtains a contrasted effect on macroscopic strength. In the zone of low mean stress (less than 6 MPa for f = 20%, less than 11 MPa for f = 15%), there is a strengthening effect by the presence of inclusions. Otherwise, the materials are rather weakened by the addition of inclusions. It seems that in this situation, the interaction between pores and inclusions enhances the plastic deformation of solid matrix. Such a weakening effect is more significant for a high value of porosity. For the case of f = 20%, one even gets a closed failure surface like pure porous materials.

5. Concluding remarks

In this paper, a series of direct numerical simulations have first been performed by a FFT-based method on heterogeneous materials

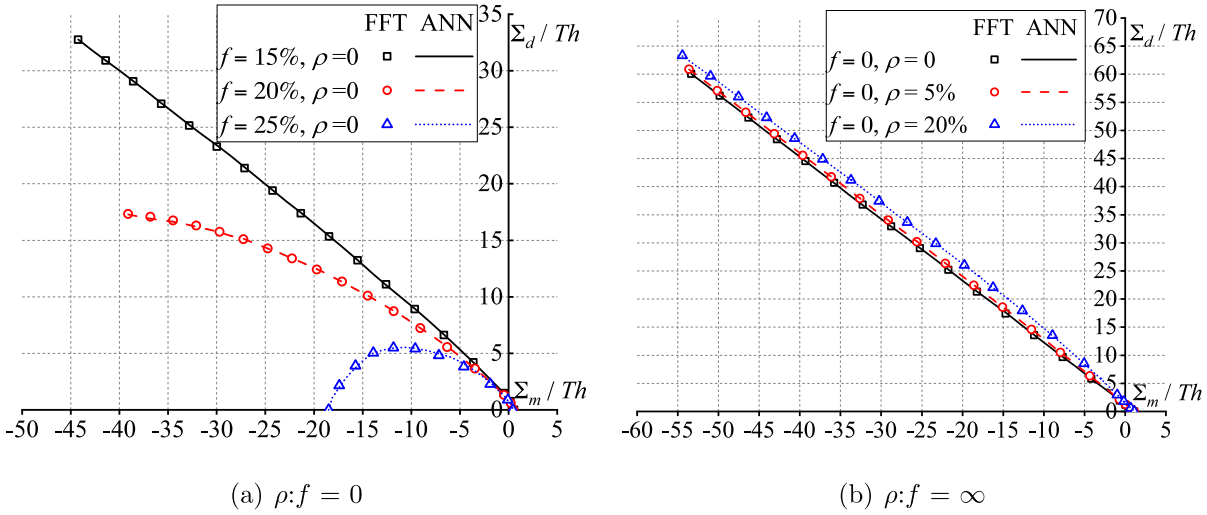

Fig. 18. Illustration of normalized macroscopic strength surface for different values of porosity for porous materials (left figure) and of inclusion volume fraction for reinforced composites (right figure): comparisons between ANN model and direct FFT simulation.

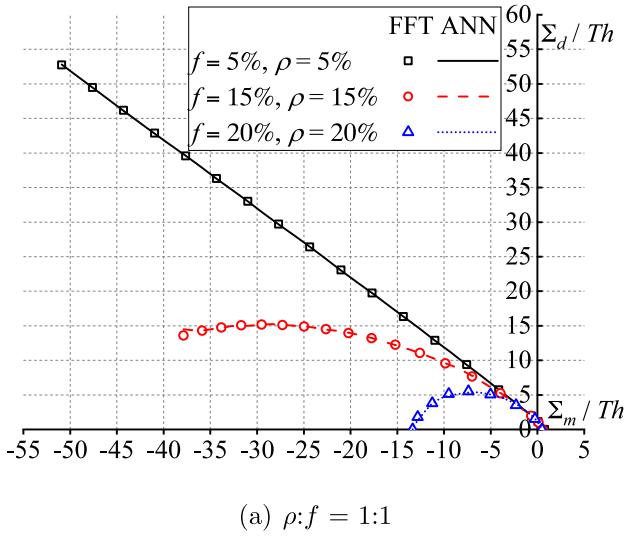

Fig. 19. Normalized macroscopic strength locus for different values of porosity and inclusion fraction with ρ: f = 1:1.

with different microstructures. In particular, three representative materials are considered: porous media, inclusion-reinforced composites and materials containing both pores and inclusions at the same scale. The results from the direct simulations are first used for investigating the macroscopic failure strength of those materials, and then to construct a representative dataset for the training and validation of an ANN-based model. This one is based on a BP algorithm and contains two hidden layers with 100 neurons in each one. The performance of the ANN model is evaluated through various statistical metrics comparisons with the reference solutions provided by the direct FFT simulations. The following main remarks can be formulated:

At the material scale considered here, the effect of pores size on macroscopic failure strength of materials is negligible. In general, the porosity has a weakening impact while the stiff inclusions have a strengthening effect. However, the influence of pores is much more important than that of inclusions. Due to the interaction between pores and inclusions, the strengthening effect of stiff inclusions is completely attenuated by the presence of pores. A weakening impact of inclusions can be observed under high values of mean stress.

The accuracy of ANN-base model is very high in predicting the macroscopic failure stresses of all types of heterogeneous materials considered here. More precisely, its accuracy is over 99% in the training (R^2 = 0.99999), validation (R^2 = 0.99992) and testing (R^2 = 0.99997) dataset. The values of RMSE (training = 0.27446, validation = 0.71933 and testing = 0.45124) also show a very good precision. And all other error indices are also very low.

In the current ANN model, we only incorporate two input microstructural parameters: porosity and inclusion volume fraction. Future investigations could expand this model to encompass additional materials parameters, such as local cohesion and friction of the solid matrix, and interface transition zone. Moreover, exploring the potential of 3D printing technology for constructing microstructure models and experimental validation represents a promising avenue for future research. Additionally, considering a convolutional neural network (CNN) approach could facilitate establishing the connection between real microstructure images and macroscopic failure strength. Another important feature is on the uncertainty of microstructure parameters, in particular for geomaterials. For this purpose, the present model should be incorporating uncertainty analysis in the ANN model.

CRediT authorship contribution statement

Jing Xue: Writing – original draft, Investigation. **Yajun Cao:** Validation, Software, Investigation. **Zhenyu Yin:** Validation, Supervision, Methodology. **Jianfu Shao:** Writing – review & editing, Supervision, Methodology, Investigation, Conceptualization. **Nicolas Burlion:** Conceptualization, Data curation, Methodology.

Declaration of competing interest

The authors declare that they have no known competing financial interests or personal relationships that could have appeared to influence the work reported in this paper.

Data availability

Data will be made available on request.

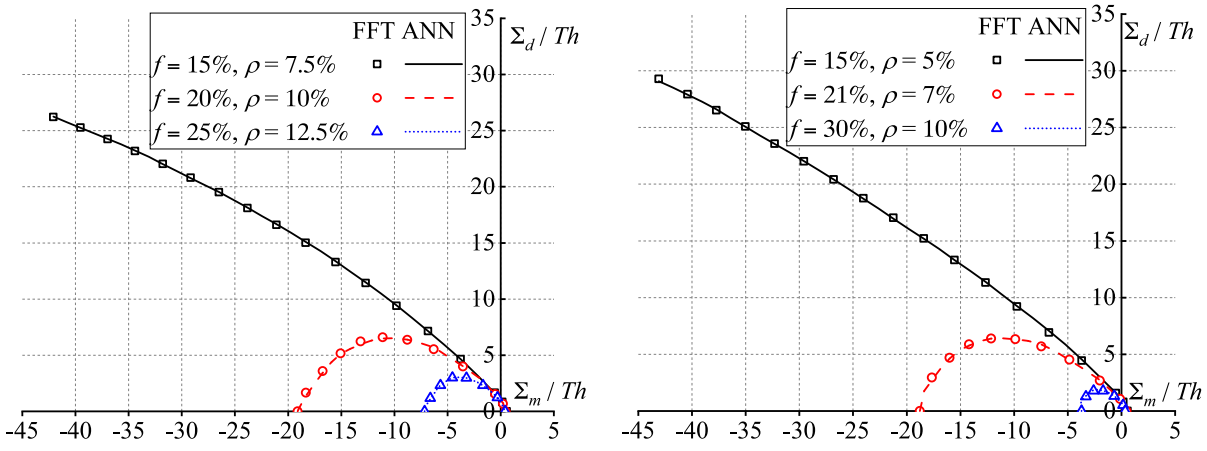

(a) ρ:f = 1:2 (b) ρ:f =1:3

Fig. 20. Normalized macroscopic strength surfaces with different values of porosity and inclusion fraction for materials containing more pores than inclusions.

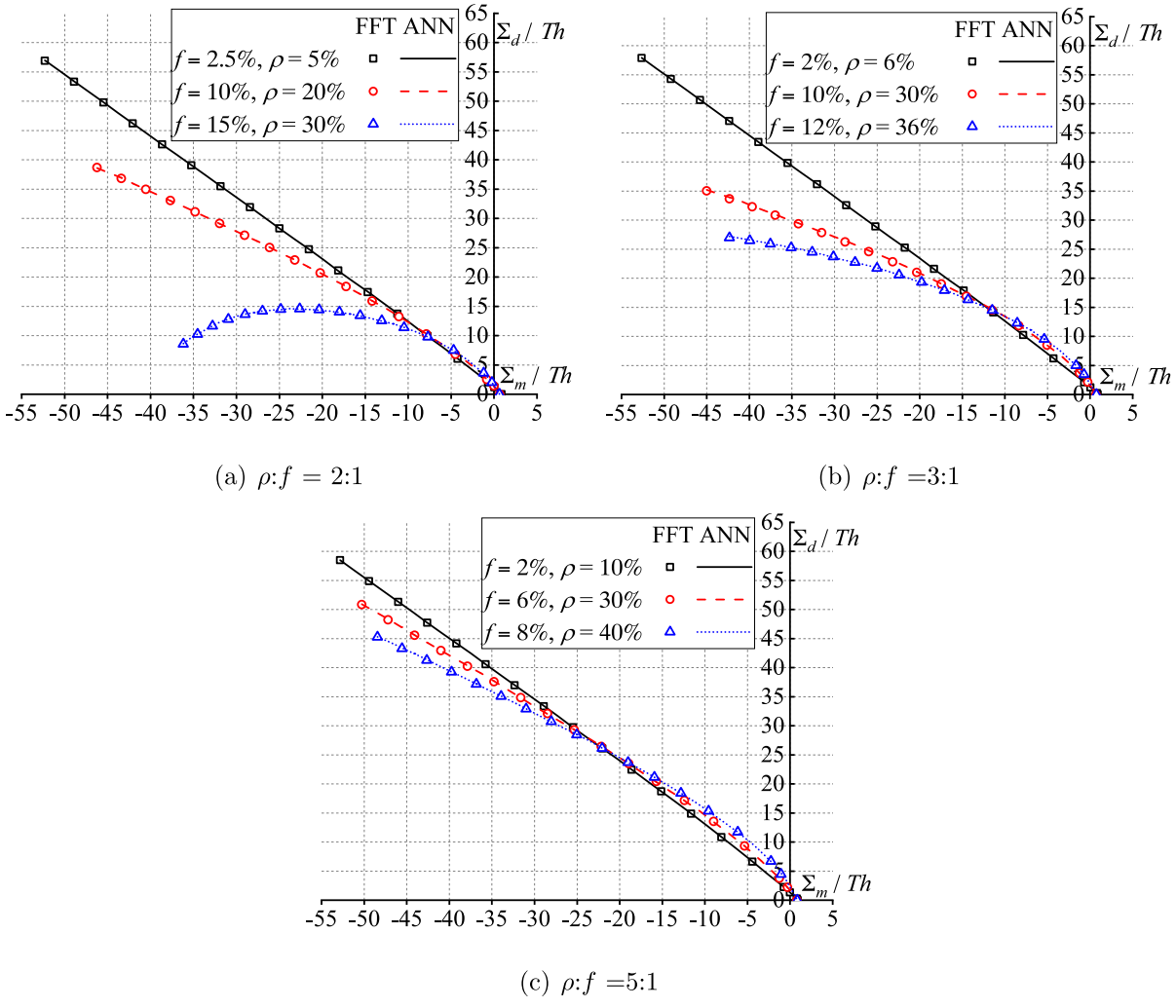

(a) ρ:f = 2:1 (b) ρ:f =3:1

(c) ρ:f =5:1

Fig. 21. Normalized macroscopic strength surfaces with different values of porosity and inclusion volume fraction for materials with more inclusions than pores.

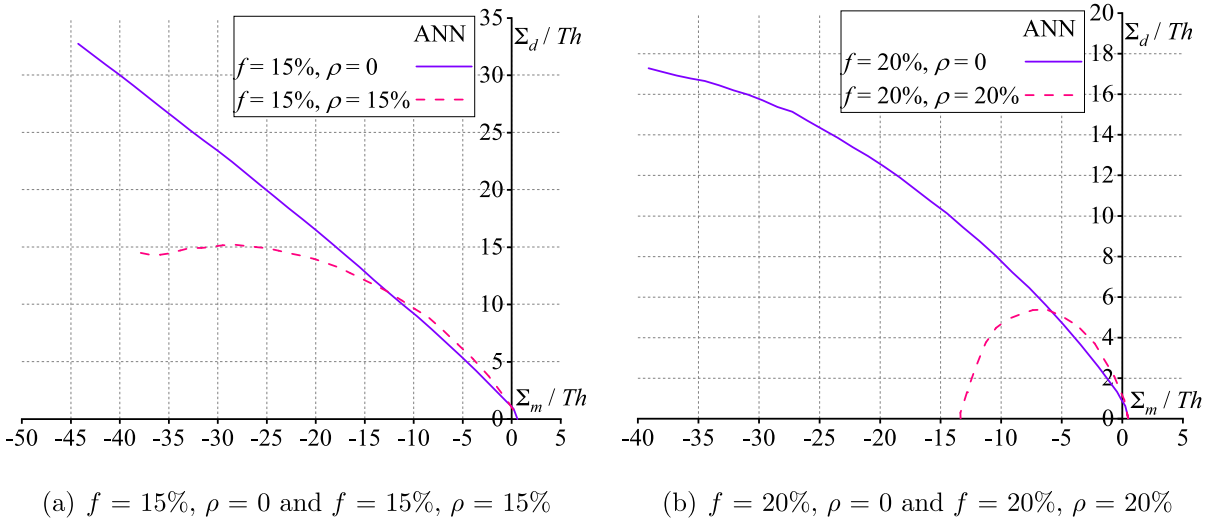

(a) $f = 15\%$, $\rho = 0$ and $f = 15\%$, $\rho = 15\%$ (b) $f = 20\%$, $\rho = 0$ and $f = 20\%$, $\rho = 20\%$

Fig. 22. Effect of inclusion volume fraction on the normalized macroscopic strength surface of materials with a given porosity.

Acknowledgments

This work has been partially supported by the European Commission project EURAD through the work package MAGIC. This is gratefully acknowledged.

References

Adesanya, E., Aladejare, A., Adediran, A., Lawal, A., Illikainen, M., 2021. Predicting shrinkage of alkali-activated blast furnace-fly ash mortars using artificial neural network (ANN). Cem. Concr. Compos. 124, 104265.

Apostolopoulou, M., Armaghani, D.J., Bakolas, A., Douvika, M.G., Moropoulou, A., Asteris, P.G., 2019. Compressive strength of natural hydraulic lime mortars using soft computing techniques. Procedia Struct. Integr. 17, 914–923.

Armaghani, D.J., Asteris, P.G., 2021. A comparative study of ANN and ANFIS models for the prediction of cement-based mortar materials compressive strength. Neural Comput. Appl. 33 (9), 4501–4532.

Armaghani, D.J., Mohamad, E.T., Narayanasamy, M.S., Narita, N., Yagiz, S., 2017. Development of hybrid intelligent models for predicting TBM penetration rate in hard rock condition. Tunn. Undergr. Space Technol. 63, 29–43.

Asteris, P.G., Ashrafian, A., Rezaie-Balf, M., 2019. Prediction of the compressive strength of self-compacting concrete using surrogate models. Comput. Concr. 24 (2), 137–150.

Asteris, P.G., Mokos, V.G., 2020. Concrete compressive strength using artificial neural networks. Neural Comput. Appl. 32 (15), 11807–11826.

Asteris, P.G., Skentou, A.D., Bardhan, A., Samui, P., Pilakoutas, K., 2021. Predicting concrete compressive strength using hybrid ensembling of surrogate machine learning models. Cem. Concr. Res. 145, 106449.

Brach, S., Dormieux, L., Kondo, D., Vairo, G., 2017. Nanoporous materials with a general isotropic plastic matrix: Exact limit state under isotropic loadings. Int. J. Plast. 89, 1–28.

Burke, H.B., Goodman, P.H., Rosen, D.B., Henson, D.E., Weinstein, J.N., Harrell Jr., F.E., Marks, J.R., Winchester, D.P., Bostwick, D.G., 1997. Artificial neural networks improve the accuracy of cancer survival prediction. Cancer 79 (4), 857–862.

Cao, Y., Shen, W., Burlion, N., Shao, J.F., 2018. Effects of inclusions and pores on plastic and viscoplastic deformation of rock-like materials. Int. J. Plast. 108, 107–124.

Cao, Y., Shen, W., Shao, J.F., Wang, W., 2020. Numerical homogenization of elastic properties and plastic yield stress of rock-like materials with voids and inclusions at same scale. Eur. J. Mech. A Solids 81, 103958.

Cao, Y., Shen, W., Shao, J.F., Wang, W., 2021. A multi-scale model of plasticity and damage for rock-like materials with pores and inclusions. Int. J. Rock Mech. Min. Sci. 138, 104579.

Cazacu, O., Ionescu, I.R., Yoon, J.W., 2010. Orthotropic strain rate potential for the description of anisotropy in tension and compression of metals. Int. J. Plasticity 26 (6), 887–904.

Chawla, K., Raju, B., Subbappa, D.B., Kancherla, K.B., Roy Mahapatra, D., 2021. Micromechanical effect of pores on elastic properties of polymer matrix composites. Polym. Compos. 42 (3), 1497–1518.

Chen, H., Asteris, P.G., Jahed Armaghani, D., Gordan, B., Pham, B.T., 2019. Assessing dynamic conditions of the retaining wall: Developing two hybrid intelligent models. Appl. Sci. 9 (6), 1042.

Chung, S., Abbott, L., 2021. Neural population geometry: An approach for understanding biological and artificial neural networks. Curr. Opin. Neurobiol. 70, 137–144.

Congro, M., de Alencar Monteiro, V.M., Brandão, A.L., dos Santos, B.F., Roehl, D., de Andrade Silva, F., 2021. Prediction of the residual flexural strength of fiber reinforced concrete using artificial neural networks. Constr. Build. Mater. 303, 124502.

Duan, J., Asteris, P.G., Nguyen, H., Bui, X.-N., Moayedi, H., 2021. A novel artificial intelligence technique to predict compressive strength of recycled aggregate concrete using ICA-XGBoost model. Eng. Comput. 37 (4), 3329–3346.

Fresca, S., Dede, L., Manzoni, A., 2021. A comprehensive deep learning-based approach to reduced order modeling of nonlinear time-dependent parametrized PDEs. J. Sci. Comput. 87 (2), 1–36.

Gărăjeu, M., Suquet, P., 1997. Effective properties of porous ideally plastic or viscoplastic materials containing rigid particles. J. Mech. Phys. Solids 45 (6), 873–902.

Ghorbanbeigi, H., Shen, W.Q., Yurtdas, I., Shao, J.F., 2016. A micromechanics-based model for concrete materials subjected to carbonation.. Int. J. Numer. Anal. Methods Geomech. 40, 1203–1218.

Gologanu, M., Leblond, J.B., Devaux, J., 1993. Approximate models for ductile metals containing non-spherical voids—case of axisymmetric prolate ellipsoidal cavities. J. Mech. Phys. Solids 41 (11), 1723–1754.

Gül, E., Ozdemir, E., Sarıcı, D.E., 2021. Modeling uniaxial compressive strength of some rocks from turkey using soft computing techniques. Measurement 171, 108781.

Gulli, A., Pal, S., 2017. Deep Learning with Keras. Packt Publishing Ltd.

Gurson, A.L., 1977. Continuum theory of ductile rupture by void nucleation and growth: Part I—Yield criteria and flow rules for porous ductile media.

Hajihassani, M., Abdullah, S.S., Asteris, P.G., Armaghani, D.J., 2019. A gene expression programming model for predicting tunnel convergence. Appl. Sci. 9 (21), 4650.

Han, J., Jentzen, A., et al., 2017. Deep learning-based numerical methods for high-dimensional parabolic partial differential equations and backward stochastic differential equations. Commun. Math. Stat. 5 (4), 349–380.

Han, B., Shen, W.Q., Xie, S.Y., Shao, J.F., 2020. Plastic modeling of porous rocks in drained and undrained conditions. Comput. Geotech. 117, 103277.

He, Z., Dormieux, L., Kondo, D., 2013. Strength properties of a Drucker–Prager porous medium reinforced by rigid particles. Int. J. Plast. 51, 218–240.

Heidenreich, J.N., Gorji, G.M.B., Dirk, M., 2023. Modeling structure-property relationships with convolutional neural networks: Yield surface prediction based on microstructure images. Int. J. Plast. 163, 103506.

Hesthaven, J.S., Ubbiali, S., 2018. Non-intrusive reduced order modeling of nonlinear problems using neural networks. J. Comput. Phys. 363, 55–78.

Huang, L., Asteris, P.G., Koopialipoor, M., Armaghani, D.J., Tahir, M., 2019. Invasive weed optimization technique-based ANN to the prediction of rock tensile strength. Appl. Sci. 9 (24), 5372.

Jain, A.K., Mao, J., Mohiuddin, K.M., 1996. Artificial neural networks: A tutorial. Computer 29 (3), 31–44.

Lawal, A.I., Aladejare, A.E., Onifade, M., Bada, S., Idris, M.A., 2021. Predictions of elemental composition of coal and biomass from their proximate analyses using ANFIS, ANN and MLR. Int. J. Coal Sci. Technol. 8 (1), 124–140.

Le, B., Yvonnet, J., He, Q.C., 2015. Computational homogenization of nonlinear elastic materials using neural networks. Internat. J. Numer. Methods Engrg. 104 (12), 1061–1084.

Lee, S.-C., 2003. Prediction of concrete strength using artificial neural networks. Eng. Struct. 25 (7), 849–857.

Lee, K., Carlberg, K.T., 2020. Model reduction of dynamical systems on nonlinear manifolds using deep convolutional autoencoders. J. Comput. Phys. 404, 108973.
Li, X., Qin, D., Hu, Y., Ahmad, W., Ahmad, A., Aslam, F., Joyklad, P., 2022. A systematic review of waste materials in cement-based composites for construction applications. J. Build. Eng. 45, 103447.
Liu, Q.f., Iqbal, M.F., Yang, J., Lu, X.-y., Zhang, P., Rauf, M., 2021. Prediction of chloride diffusivity in concrete using artificial neural network: Modelling and performance evaluation. Constr. Build. Mater. 268, 121082.
Logarzo, H.J., Capuano, G., Rimoli, J.J., 2021. Smart constitutive laws: Inelastic homogenization through machine learning. Comput. Methods Appl. Mech. Engrg. 373, 113482.
Ma, X., Pan, J., Cai, J., Zhang, Z., Han, J., 2021. A review on cement-based materials used in steel structures as fireproof coating. Constr. Build. Mater. 125623.
Ma, Z., Zhang, B., 2023. Deep learning based upscaling of geomechanical constitutive behavior for lithological heterogeneities. In: SPE Annual Technical Conference and Exhibition?. SPE, D031S032R002.
Maghous, S., Dormieux, L., Barthèlèmy, J.F., 2009. Micromechanical approach to the strength properties of frictional geomaterials. Eur. J. Mech. A/Solid 28, 179–188.
Monchiet, V., Cazacu, O., Charkaluk, E., Kondo, D., 2008. Macroscopic yield criteria for plastic anisotropic materials containing spheroidal voids. Int. J. Plast. 24 (7), 1158–1189.
Monchiet, V., Charkaluk, E., Kondo, D., 2014. Macroscopic yield criteria for ductile materials containing spheroidal voids: An Eshelby-like velocity fields approach. Mech. Mater. 72, 1–18.
Monchiet, V., Kondo, D., 2013. Combined voids size and shape effects on the macroscopic criterion of ductile nanoporous materials. Int. J. Plast. 43, 20–41.
Moulinec, H., Suquet, P., 1994. A fast numerical method for computing the linear and nonlinear mechanical properties of composites. C. R. de l'Acad. des Sci.. Sér. II. Méc., Phys., Chimie, Astronomie.
Moulinec, H., Suquet, P., 1998. A numerical method for computing the overall response of nonlinear composites with complex microstructure. Comput. Methods Appl. Mech. Engrg. 157 (1–2), 69–94.
Murakami, Y., Endo, M., 1994. Effects of defects, inclusions and inhomogeneities on fatigue strength. Int. J. Fatigue 16 (3), 163–182.
N'souglo, K.E., Rodríguez-Martínez, J.A., Cazacu, O., 2020. The effect of tension-compression asymmetry on the formation of dynamic necking instabilities under plane strain stretching. Int. J. Plast. 128, 102656.
Piemaan, F., Whan, Y.J., 2023. Machine learning-driven stress integration method for anisotropic plasticity in sheet metal forming. Int. J. Plast. 166, 103642.
Qazi, A., Fayaz, H., Wadi, A., Raj, R.G., Rahim, N., Khan, W.A., 2015. The artificial neural network for solar radiation prediction and designing solar systems: A systematic literature review. J. Clean. Prod. 104, 1–12.
Raissi, M., Perdikaris, P., Karniadakis, G.E., 2019. Physics-informed neural networks: A deep learning framework for solving forward and inverse problems involving nonlinear partial differential equations. J. Comput. Phys. 378, 686–707.
Ray, D., Hesthaven, J.S., 2018. An artificial neural network as a troubled-cell indicator. J. Comput. Phys. 367, 166–191.
Robinet, J.C., Sardini, P., Coelho, D., Parneix, J.C., Pret, D., Sammartino, S., Boller, E., Altmann, S., 2012. Effects of mineral distribution at mesoscopic scale on solute diffusion in a clay-rich rock: Example of the Callovo-Oxfordian mudstone (Bure, France). Water Resour. Res. 48, W05554.
Santos, I., Castro, L., Rodriguez-Fernandez, N., Torrente-Patino, A., Carballal, A., 2021. Artificial neural networks and deep learning in the visual arts: A review. Neural Comput. Appl. 33 (1), 121–157.
Shaoheng, G., Xue, Z., Sascha, R., Tongming, Q., 2023. A neural network-based material cell for elastoplasticity and its performance in FE analyses of boundary value problems.. Int. J. Plast. 171, 103811.
Shen, W., 2022. Approximate plastic yield criteria of geomaterials with pores and grains embedded in a porous matrix. Int. J. Plast. 153, 103275.
Shen, W., He, Z., Dormieux, L., Kondo, D., 2014. Effective strength of saturated double porous media with a Drucker–Prager solid phase. Int. J. Numer. Anal. Methods Geomech. 38 (3), 281–296.
Shen, W., Kondo, D., Dormieux, L., Shao, J.F., 2013. A closed-form three scale model for ductile rocks with a plastically compressible porous matrix. Mech. Mater. 59, 73–86.
Shen, W., Shao, J.F., Kondo, D., Gatmiri, B., 2012. A micro–macro model for clayey rocks with a plastic compressible porous matrix. Int. J. Plasticity 36, 64–85.
Shen, W.Q., Shao, J.F., liu, Z.B., Oueslati, A., DeSaxce, G., 2020. Evaluation and improvement of macroscopic yield criteria of porous media having a Drucker-Prager matrix. Int. J. Plast. 126, 102609.
Shukla, N., Fricklas, K., 2018. Machine Learning with TensorFlow. Manning Greenwich.
Sirignano, J., Spiliopoulos, K., 2018. DGM: A deep learning algorithm for solving partial differential equations. J. Comput. Phys. 375, 1339–1364.
Stock, A., Hannantt, D., Williams, R., 1979. The effect of aggregate concentration upon the strength and modulus of elasticity of concrete. Mag. Concrete Res. 31 (109), 225–234.
Tam, V.W., Butera, A., Le, K.N., Da Silva, L.C., Evangelista, A.C., 2022. A prediction model for compressive strength of CO2 concrete using regression analysis and artificial neural networks. Constr. Build. Mater. 324, 126689.
Vasilyeva, M., Leung, W.T., Chung, E.T., Efendiev, Y., Wheeler, M., 2020. Learning macroscopic parameters in nonlinear multiscale simulations using nonlocal multicontinua upscaling techniques. J. Comput. Phys. 412, 109323.
Vasilyeva, M., Tyrylgin, A., 2021. Machine learning for accelerating macroscopic parameters prediction for poroelasticity problem in stochastic media. Comput. Math. Appl. 84, 185–202.
Vincent, P.G., Monerie, Y., Suquet, P., 2009. Porous materials with two populations of voids under internal pressure: I. Instantaneous constitutive relations. Int. J. Solids Struct. 46 (3–4), 480–506.
Xie, S.Y., Shao, J.F., 2006. Elastoplastic deformation of a porous rock and water interaction. Int. J. Plast. 22, 2195–2225.
Xie, S.Y., Shao, J.F., 2012. Experimental investigation and poroplastic modeling of saturated porous geomaterials. Int. J. Plast. 39, 27–45.
Xue, J., Cao, Y.J., Burlion, N., Shao, J.F., 2023a. Influence of interface transition zone on effective elastic property of heterogeneous materials with an artificial neural network study. Int. J. Numer. Anal. Methods Geomech. 47 (7), 1134–1151.
Xue, J., Cao, Y.J., Shao, J.F., Burlion, N., 2023b. Study of effective elastic properties of heterogeneous materials with an artificial neural network model. Mech. Mater. 104597.
Xue, J., Shao, J., Burlion, N., 2021. Estimation of constituent properties of concrete materials with an artificial neural network based method. Cem. Concr. Res. 150, 106614.
Yang, H., Koopialipoor, M., Armaghani, D.J., Gordan, B., Khorami, M., Tahir, M., 2019. Intelligent design of retaining wall structures under dynamic conditions. Steel Composite Struct., Int. J. 31 (6), 629–640.
Zailan, S.N., Mahmed, N., Abdullah, M.M.A.B., Rahim, S.Z.A., Halin, D.S.C., Sandu, A.V., Vizureanu, P., Yahya, Z., 2022. Potential applications of geopolymer cement-based composite as self-cleaning coating: A review. Coatings 12 (2), 133.
Zhang, B., Ma, Z., Zheng, D., Chalaturnyk, R.J., Boisvert, J., 2023. Upscaling shear strength of heterogeneous oil sands with interbedded shales using artificial neural network. SPE J. 28 (02), 737–753.